# Inverted chimeric RNAi molecules synergistically co-target MYC and KRAS in KRAS-driven cancers

Yogitha S Chareddy, … , Martin Egli, Chad V. Pecot

**Research** In-Press Preview Oncology

Mutant KRAS has been implicated in driving a quarter of all cancer types. Although inhibition of the KRAS$^{G12C}$ mutant protein has shown clinical promise, there is still a need for therapies that overcome resistance and target non-KRAS$^{G12C}$ mutations. KRAS activates downstream MYC, which is also a challenging-to-drug oncoprotein. We have developed an "inverted" RNAi molecule with the passenger strand of a MYC-targeting siRNA fused to the guide strand of a KRAS-targeting siRNA. The chimeric molecule simultaneously inhibits KRAS and MYC, showing marked improvements in efficacy beyond the individual siRNA components. This effect is mediated by 5'-dT overhangs following endosomal metabolism. The synergistic RNAi activity led to a >10-40-fold improvement in inhibiting cancer viability in vitro. When conjugated to an epidermal growth factor receptor (EGFR)-targeting ligand, the chimeric siRNA was delivered to and internalized by tumor cells. As compared with individual targeting siRNAs, the chimeric design resulted in considerably improved metabolic stability in tumors, enhanced silencing of both oncogenes, and reduced tumor progression in multiple cancer models. This inverted chimeric design establishes proof-of-concept for ligand-directed, dual-silencing of KRAS and MYC in cancer and constitutes an innovative molecular strategy for co-targeting any two genes of interest, which has broad implications.

**Find the latest version:**

https://jci.me/187204/pdf

1    **Inverted chimeric RNAi molecules synergistically co-target MYC and KRAS in KRAS-**

2    **driven cancers**

3    **Authors:** Yogitha S. Chareddy[1,2], Hayden P. Huggins[2,3], Snehasudha S. Sahoo[2], Lyla J.

4    Stanland[3], Christina Gutierrez-Ford[2], Kristina Whately[2], Lincy Edatt[2], Salma H. Azam[2], Matthew

5    C. Fleming[4,5], Jonah Im[2], Alessandro Porrello[2,6], Imani Simmons[2], Jillian L. Perry[7,8], Albert A.

6    Bowers[4,5,9], Martin Egli[10], Chad V. Pecot[2,6,11,12]

7

8    **Affiliations:**

9    [1]Curriculum in Genetics and Molecular Biology, University of North Carolina at Chapel Hill (UNC-

10   CH), Chapel Hill, NC, USA.

11   [2]Lineberger Comprehensive Cancer Center, UNC-CH.

12   [3]EnFuego Therapeutics, Inc, Morrisville, NC, USA.

13   [4]Division of Chemical Biology and Medicinal Chemistry, Eshelman School of Pharmacy, UNC-

14   CH.

15   [5]Center for Integrative Chemical Biology and Drug Discovery, Eshelman School of Pharmacy,

16   UNC-CH.

17   [6]RNA Discovery Center, UNC-CH.

18   [7]Division of Pharmacoengineering and Molecular Pharmaceutics, Eshelman School of Pharmacy,

19   UNC-CH.

20   [8]Center for Nanotechnology in Drug Delivery, UNC-CH.

21   [9]Department of Chemistry, UNC-CH.

22   [10]Department of Biochemistry, School of Medicine, Vanderbilt University, Nashville, TN, USA

23   [11]Division of Oncology, UNC-CH.

24   [12]Department of Medicine, UNC-CH.

25

26

27    **Corresponding Author**:

28    Chad V. Pecot,

29    450 West Drive, Chapel Hill, NC, USA 27312

30    pecot@email.unc.edu

31    (+1) 615-305-3955

32

37

**Abstract**

Mutant KRAS has been implicated in driving a quarter of all cancer types. Although inhibition of the KRAS$^{G12C}$ mutant protein has shown clinical promise, there is still a need for therapies that overcome resistance and target non-KRAS$^{G12C}$ mutations. KRAS activates downstream MYC, which is also a challenging-to-drug oncoprotein. We have developed an "inverted" RNAi molecule with the passenger strand of a MYC-targeting siRNA fused to the guide strand of a KRAS-targeting siRNA. The chimeric molecule simultaneously inhibits KRAS and MYC, showing marked improvements in efficacy beyond the individual siRNA components. This effect is mediated by 5'-dT overhangs following endosomal metabolism. The synergistic RNAi activity led to a >10-40-fold improvement in inhibiting cancer viability in vitro. When conjugated to an epidermal growth factor receptor (EGFR)-targeting ligand, the chimeric siRNA was delivered to and internalized by tumor cells. As compared with individual targeting siRNAs, the chimeric design resulted in considerably improved metabolic stability in tumors, enhanced silencing of both oncogenes, and reduced tumor progression in multiple cancer models. This inverted chimeric design establishes proof-of-concept for ligand-directed, dual-silencing of KRAS and MYC in cancer and constitutes an innovative molecular strategy for co-targeting any two genes of interest, which has broad implications.

**Introduction**

Mutations in the GTPase KRAS are responsible for driving nearly 25% of all cancers (1, 2). Normally involved in cell proliferation and differentiation, the *KRAS* proto-oncogene is often mutated at amino acid positions 12 and 13, which constitutively activates the KRAS protein by locking it into the active GTP-bound state (3). Until recently, KRAS was largely considered an "undruggable" target because the surface topology of the protein did not present a binding interface for a traditional small molecule inhibitor (4, 5). However, studies have shown that the KRAS[G12C] mutant form can create a stable nucleophilic binding pocket that can be targeted with covalent small-molecule inhibitors (6). This has led to the rapid development of clinical stage KRAS[G12C] inhibitors (7-9), including approved drugs sotorasib and adagrasib. Although KRAS[G12C] inhibitors sotorasib and adagrasib resulted in response rates of ~40% in lung cancer patients (10, 11), various mechanisms of resistance have been observed, including secondary KRAS mutations (12-17). Furthermore, KRAS[G12C] only accounts for approximately 12% of all KRAS mutations (8, 9, 18, 19). While direct KRAS[G12C] inhibitors have proven KRAS is druggable with clinically meaningful responses, there remains an urgent need for innovative molecules that can 1) target non-KRAS[G12C] mutations, and 2) can overcome the many resistance mechanisms frequently observed with KRAS targeting.

Several studies have shown that mutant KRAS cooperates with the proto-oncogene, c-Myc (MYC), in promoting and maintaining aggressive tumorigenesis through several mechanisms, including stimulation of inflammation, activation of pro-survival pathways, and suppression of apoptosis (20-22). Importantly, MYC upregulation has been found to be a key mediator in promoting resistance to KRAS inhibition (16, 23-25). MYC is a transcription factor that has critical roles in homeostasis and regulates ~15% of the genome (26). Importantly, MYC is regarded as a critical oncoprotein and is dysregulated in approximately 50-70% of cancers (26). Several studies have shown that downregulation and/or inactivation of MYC can substantially inhibit tumorigenesis, making it a very attractive therapeutic target (27-30). Like most KRAS-

4

81    mutant proteins, MYC does not have any approved targeted therapies despite its intensive

82    characterization, which is in part due to its unstructured domains, inaccessible localization in the

83    nucleus, and ubiquitous expression in healthy tissues (4). Current therapeutic strategies for

84    targeting MYC include targeting MYC/Max heterodimer, use of a dominant negative MYC mimic,

85    or by targeting downstream genes (31-35). However, others have shown that targeting MYC alone

86    may not be sustainable as it may result in toxicity, or cancer cells may quickly evolve to reactivate

87    it (36-38).

88        KRAS activation can stabilize MYC either by initiating the phosphorylation of MYC at

89    serine 62 via ERK1/2 signaling or by preventing the phosphorylation of MYC at threonine 58 via

90    inhibition of GSK3β, which usually targets MYC protein for degradation (39). In KRAS-mutant

91    pancreatic cancer, MYC stabilization can also occur following ERK1/2 inhibition via the activation

92    of the alternative MEK5/-ERK5 pathway (40). Inhibition of MYC can sensitize cancer cells to

93    cytotoxins and promote tumor regression and increased survival in mice (34, 41). These data

94    strongly imply that the dual suppression of mutant KRAS and MYC may lead to a synergistic

95    anticancer effect. Indeed, several independent studies using transgenic mouse models have

96    shown that losing both oncogenes can lead to a greater reduction in tumor burden and enhanced

97    survival in breast and lung cancer (42, 43).

98        RNA interference (RNAi)-based therapies present a unique alternative strategy for

99    targeting "undruggable" proteins like MYC and KRAS and operate through the RNA-induced

100   silencing complex (RISC) (44). Briefly, cytosolic RISC unwinds delivered dsRNA and loads the

101   guide strand to recognize and cleave complementary mRNA sequences (44). Although RNAi is

102   sequence-specific and potent, up until recently it has faced several clinical obstacles, including in

103   vivo instability, lack of tissue-specific delivery, off-target silencing effects, and immunogenicity

104   (45). However, recent innovations in the RNAi therapeutics field have led to the adoption of

105   receptor-targeting ligands conjugated to fully chemically modified siRNAs (45). These advances

106   have helped overcome many physiologic barriers, leading to several clinically approved RNAi-

107    based drugs that silence mRNA targets in the liver (46-48). Although similar ligand-conjugated

108    RNAi approaches have yet to succeed in the context of cancer treatment, there are several

109    developing platforms that show good safety profiles and anti-tumor efficacy signals (49-51). Here,

110    we describe what we believe to be novel compositions of inverted RNAi molecules that exhibit

111    unexpectedly potent co-silencing of MYC and KRAS. These inverted RNAi molecules showed up

112    to a 40-fold improvement in inhibition of cancer cell viability. Importantly, these chimeric designs

113    may be broadly applicable for co-silencing any two target genes of interest, which has far-reaching

114    implications for cancer and beyond.

115

116

## Results

### Identification of potent, chemically modified MYC and pan-KRAS siRNAs

To identify *MYC*-targeting siRNA sequences, we analyzed human and mouse *MYC* sequences for conserved regions. Using several open-source design tools, we identified eight sequences with high predicted efficacy against *MYC* (Supplemental Table 1), which target the highly conserved open reading frames of human and mouse *MYC* (Supplemental Figure 1A). We initially evaluated these sequences as unmodified siRNAs with 3' deoxythymidine (dTdT) overhangs.

We transfected these siRNAs into MIA PaCa-2 pancreatic carcinoma cells (KRAS$^{G12C}$/WT) to identify the most potent based on reduced *MYC* mRNA and protein expression. Compared to a non-targeting control (NC) siRNA, sequences 1, 2, 4, 6, and 8 greatly reduced *MYC* mRNA levels by 24- and 48-hours post-transfection (Supplemental Figure 1B), and MYC protein levels by 24 hours (Supplemental Figure 1C).

To confer drug-like properties to the siRNAs (52), we included 2'-O-methyl and 2'-fluoro modifications on the sugar moieties, and phosphorothioates at the 5'- and 3'-ends of each strand in order to avoid endo- and exo-nuclease degradation, respectively. These chemical modifications have been shown to reduce immunogenicity and off-target effects and increase stability in vivo without marked reductions in efficacy (45, 53). For initial screening, we chose a higher 2'-fluoro (Hi2F) design. We tested the chemically modified versions of our top five candidates from the unmodified screen using MIA PaCa-2 and A427 (KRAS$^{G12D}$/WT) lung carcinoma cells. Compared with NC siRNA, modified MYC-targeting sequences 2 and 3 (Mseq2 and Mseq3) reduced up to 80% of *MYC* mRNA in both cell lines at 24, 48, and 72 hours (Supplemental Figure 2A) and MYC protein levels at 72 hours (Supplemental Figure 2B).

142　To assess anti-tumor activity, we evaluated siRNA transfection on spheroid formation to simulate

143　the tumor microenvironment. Compared to NC siRNA, Mseq2 and Mseq3 dramatically reduced

144　spheroid density in both cell lines (Supplemental Figure 2C). These data demonstrate that our

145　modified MYC siRNAs strongly silence *MYC* expression and significantly reduce tumorigenic

146　potential.

147

148　Previous efforts in our lab led to the development of potent unmodified pan-KRAS siRNAs (54).

149　Although these siRNAs demonstrated preclinical efficacy when delivered in nanoliposomes (54),

150　the use of ligand-directed, fully chemically modified siRNAs has recently reshaped the RNAi field

151　(45, 51, 52). By modifying these pan-KRAS siRNAs with a high proportion of 2'-O-methyl

152　modifications (Hi2OMe), which confers improvements in metabolic stability within the endosomal

153　compartment (55), we found that the KRAS siRNAs (Kseq2 and Kseq3) retained potent RNAi

154　activity in several cancer cell lines (Supplemental Figure 2, D and E).

155

156　**Co-Targeting with KRAS and MYC siRNAs Reduces Tumorigenic Properties in vitro**

157　Mutant KRAS signaling stabilizes and hyperactivates MYC via ERK1/2, leading to MYC

158　accumulation and sustained pro-tumorigenic signaling (Supplemental Figure 3A) (40).

159　Simultaneous inactivation of these oncogenes has been shown to synergistically decrease tumor

160　progression (42, 43).

161

162　We evaluated the effects of RNAi-mediated KRAS and MYC silencing on tumorigenesis.

163　Compared to NC siRNA and individual KRAS or MYC siRNAs, equimolar combinations of KRAS

164　and MYC siRNAs resulted in significantly reduced spheroid formation in MIA PaCa-2 cells

165　(Supplemental Figure 3B). Similar results were observed in A427, H441 (lung carcinoma;

166　KRAS$^{G12V}$/WT), and HCT116 (colorectal carcinoma; KRAS$^{G13D}$/WT) cells, and the combination of

167　Kseq2 and Mseq2 siRNAs consistently performed as the most effective treatment (Supplemental

168 Figure 3C). Our results demonstrate that dual siRNA-mediated silencing of KRAS and MYC are

169 highly effective at preventing tumorigenesis beyond either siRNA alone across several cancer

170 types and common KRAS mutations.

171

172 **Inverted Multivalent Chimeras Potently Co-Target MYC and KRAS Oncogenes**

173 To ensure equimolar targeting of two siRNAs, we considered that phosphodiester bridges can

174 confer "pro-drug" like activity in the plasma and allow for endo-nucleolytic metabolism within the

175 target tissue (56). We developed two conformations of the KRAS and MYC chimera using a DNA

176 bridge consisting of four 2'-deoxythymidines: a "serial" conformation linking the MYC and KRAS

177 guide strands, and an "inverted" conformation linking the MYC passenger to the KRAS guide

178 strand (Figure 1A). Mseq2 Hi2F and Kseq2 Hi2OMe modified siRNAs were used in preliminary

179 chimera designs (M2/K2 Chimera V1).

180

181 To test the chimeric siRNA designs, we evaluated equimolar transfections of the siRNAs at

182 various doses and time points. Although both chimeric designs improved potency, we found that

183 M2/K2 Inverted Chimera V1 was more potent at silencing both *MYC* and *KRAS* than M2/K2 Serial

184 Chimera V1 (Figure 1B). M2/K2 Inverted Chimera V1 was also consistently as effective or better

185 than co-delivery of individual siRNAs (Figure 1C and Supplemental Figure 3D).

186

187 The enhanced potency of the inverted chimeric design was validated in additional cell lines

188 (Supplemental Figure 4, A and B). Notably, the inverted chimeric design was far more potent at

189 silencing *MYC* and *KRAS* beyond that seen with the individual siRNAs. For example, at 5 nM,

190 either of the MYC or KRAS siRNAs resulted in ~70% silencing, however, the inverted chimeric

191 design led to >90% target silencing of *KRAS* (Figure 1B and Supplemental Figure 4, A and B).

192 Similar observations were made at the protein level, where the inverted chimeric design showed

193 improved silencing compared with the serial chimeric design (Supplemental Figure 4C). Together,

9

194  these data demonstrate that the inverted chimeric siRNA is more potent than its individual siRNA

195  components in combination, and that the orientation of the individual components affects the

196  chimera's efficacy.

197

198  **Chimeric siRNAs are Metabolized Primarily in Endosomes**

199  The plasma half-life of ligand-conjugated siRNAs ranges from around 15-90 minutes, depending

200  on variables such as the conjugated ligand, linker, oligonucleotide modifications, and delivery

201  routes (50, 57). Upon systemic administration, ligand-conjugated siRNAs travel through the

202  bloodstream and are directed to their intended target receptor. Upon receptor engagement, the

203  ligand and siRNA payload are internalized via clathrin-mediated endocytosis and the latter

204  eventually escapes into the cytosol to become incorporated into the RISC complex and elicit

205  RNAi-mediated target mRNA degradation (53). In the endosomal compartment, siRNAs are

206  exposed to nucleolytic enzymes, which can lead to degradation (58). To assess where these

207  chimeric siRNAs are metabolically processed, we incubated the individual MYC and KRAS

208  siRNAs and the two M2/K2 chimera designs in plasma, endosomal, and cytosolic conditions for

209  up to 24 hours. First, we tested stability in 50% serum and found that both chimera designs had

210  minimal metabolic processing after 6 hours, suggesting they would largely remain intact upon

211  target tissue exposure in vivo (57). By 24 hours, the serial chimera had undergone increased

212  cleavage compared to the inverted chimera (Figure 2A). Additionally, when comparing the two

213  chemical modification patterns, the MYC Hi2F siRNA degraded more quickly than the KRAS

214  Hi2OMe siRNA, supporting the idea of increased siRNA stability with increased 2'-OMe content

215  (59). Next, we incubated the siRNAs in acidified rat liver tritosomes as a proxy for endosomes,

216  which undergo a decrease in pH as they become lysosomes (58). While the individual MYC and

217  KRAS siRNAs remained relatively unprocessed, both chimeras underwent cleavage at the

218  thymidine bridge by 24 hours (Figure 2B). The entire chimeric structure was disrupted by 48 hours

219  (Supplemental Figure 5A). To assess whether cleavage was due to the acidic pH within the

220    endosome, we incubated the siRNAs in an acidic buffer without tritosomes and found that the

221    chimeras remained stable for up to 48 hours (Supplemental Figure 5B), suggesting that the

222    metabolism of the chimeras is through endo-nucleolytic cleavage. We incubated the siRNAs with

223    rat liver cytosol and found they remained mostly unprocessed (Figure 2C).

224

225    During the RNAi process, the RNase type III enzyme Dicer can process long dsRNA into 21-23

226    base pair fragments (44). The chimeric siRNA constructs investigated here are 46 nucleotides

227    long, *i.e.* twice as long as the dsRNAs produced by Dicer. Therefore, we tested whether the

228    chimera could also serve as a substrate for Dicer. We directly treated the siRNAs with

229    recombinant human Dicer and found that the chimeric molecules are not processed

230    (Supplemental Figure 6A). We also evaluated knockdown efficiency by comparing dose-response

231    and kinetics between a parental HEK293T cell line and a Dicer CRISPR-knockout line (HEK293T

232    NoDice). We found no significant decrease in knockdown efficacy for either chimeric design

233    (Supplemental Figure 6, B and C). Based on these observations, we conclude that both chimeric

234    siRNA designs remain intact in plasma conditions and are predominately metabolized within the

235    endosomal compartment upon receptor-mediated endocytosis (Figure 2D).

236

237    **Chimeric Bridge Cleavage Results in More Potent 5'-Guide Overhangs**

238    Argonaute2 (Ago2) is the key enzyme in RISC responsible for mediating RNAi (45). Ago2

239    interacts with guide RNA through the MID (binds the 5'-end of a guide RNA), PIWI (induces

240    cleavage), and PAZ (anchors the 3'-end of a guide RNA) domains (45). Initial modeling assessed

241    the possibility of the full inverted chimeric strand (*i.e.* the passenger strand of Mseq2 and the

242    guide strand of Kseq2 linked by the thymidine bridge) getting loaded into Ago2 opposite the *KRAS*

243    target strand. However, using structural modeling, we determined that weaving of the linker

244    portion out of the MID/PIWI binding cleft while avoiding clashes with Ago2 side chains and/or

245    target strand residues is nearly impossible (Supplemental Figure 7, A and B). This suggests that

246     it is unlikely that the full chimeric construct is accommodated inside Ago2 opposite the target

247     mRNA, with its phosphodiester moiety between dT and the 5'-most U of Kseq2 bound in the MID

248     binding pocket like a 5'-terminal phosphate. Instead, we determined it is more likely that the KRAS

249     guide strand gets loaded into Ago2 after its 5'-end undergoes metabolic processing.

250

251     To determine the identity of the metabolic products following endosomal processing, we incubated

252     the M2/K2 Inverted Chimera in endosomal conditions for 48 hours and analyzed the samples with

253     liquid chromatography–mass spectrometry (LC-MS). We detected nearly every potential

254     metabolic product with dT overhangs, confirming cleavage at the thymidine bridge (Supplemental

255     Figure 8, A and B and Supplemental Table 2). Due to the length of incubation and differences in

256     5' and 3' exonuclease degradation dynamics, it is likely that the proportions of metabolic products

257     in our sample are not equivalent to exact cellular conditions as these molecules may undergo

258     further processing to remove the overhangs. Based on this data, we evaluated whether the

259     metabolic products of the cleaved thymidine bridge (5'-dT overhangs) could explain the potency

260     of the chimeric designs.

261

262     We utilized an A-431 KRAS CRISPR knockout line stably transduced with a KRAS-Firefly

263     luciferase reporter system to evaluate knockdown efficiency on a 10-point dose-response curve

264     (60). We observed that both chimeric designs decreased KRAS expression more potently than

265     the single KRAS siRNA, and that the inverted chimera showed the highest potency (Figure 3A).

266     To evaluate all possibilities of the thymidine bridge cleavage, with two 2'-deoxythymidine (2dT)

267     5'-terminal overhangs being the most likely (56), we tested iterations of Kseq2 with 5'-dT

268     overhangs at each thymidine position on the guide strand. We also included a "non-cleavable"

269     thymidine bridge with phosphorothioate modifications throughout to confirm that the chimera must

270     be cleaved for RNAi activity (Figure 3B). As expected, the fully modified "non-cleavable" thymidine

271     bridge showed essentially no knockdown (Figure 3C). Unexpectedly, we found that Kseq2 with

272     5'-dT overhangs on the guide strand performed better than Kseq2 alone, with increasing potency

273     directly correlated with the addition of each dT, although the increased potency plateaued at 3

274     dT.

275

276     It is possible that the potency is due to a shift in the seed region of the guide strand. To test if this

277     was the reason for the increase in potency, we created two Mseq2 and two Kseq2 siRNAs with

278     overhangs that were perfectly complementary to the target mRNA (Supplemental Figure 9A). We

279     then conducted 10-point dose-response assays to compare the effect on cell viability. We found

280     that Mseq2 2dT was still more potent than Mseq2 dTG, and there was total abolishment of activity

281     with Mseq2 dTGA (Supplemental Figure 9B). We found a similar pattern when testing Kseq2 dGT

282     and dGTG using our KRAS-luciferase reporter (Supplemental Figure 9C). Based on these data,

283     we do not believe that the improvement in potency from 5'-thymidine overhangs is related to a

284     shift in the seed region, and instead, the guide strand of Kseq2 with a 2dT overhang at the 5'-end

285     is becoming incorporated into Ago2 to induce mRNA silencing, whereby the 2dT overhang fits

286     into the MID domain binding pocket (Figure 4, A and B). Thus, the phosphodiester linkage (charge

287     -1) between Kseq2 and 2dT sits in the MID domain binding pocket normally occupied by the 5'-

288     terminal phosphate (charge -2) of guide siRNA. The two thymidines protrude into the cleft

289     between the MID and PIWI domains and can be accommodated between the guide and target

290     strands.

291

292     **Inverted MYC/KRAS Chimeras Synergistically Target KRAS Mutant Cancers**

293     To further stabilize the inverted chimera (59), we evaluated the Hi2OMe chemical modification

294     pattern on the MYC siRNAs (Supplemental Figure 10A). Knockdown efficiency of MYC siRNAs

295     with Hi2F and Hi2OMe modification patterns was similar across several cell lines, with Mseq2

296     Hi2OMe being the most potent (Supplemental Figure 10B). We incorporated this design into the

297     M2/K2 inverted chimeric siRNA to generate M2/K2 Inverted Chimera Version 2 (V2)

13

298    (Supplemental Figure 10C). Comparing M2/K2 V1 and V2 inverted chimera designs at low doses

299    showed nearly equipotent levels of MYC and KRAS silencing (Supplemental Figure 10D),

300    suggesting M2/K2 Inverted Chimera V2 experiences no loss of potency while having improved

301    metabolic stability conferred by additional 2'OMe modifications in vivo. Modeling full M2/K2

302    Inverted Chimera V2 in silico revealed that the thymidine bridge is flexible and that the linked

303    siRNAs likely have a dynamic orientation to each other (Figure 5, A and B).

304

305    We found that M2/K2 Inverted Chimera V2 has far more potency than the individual siRNAs

306    across several doses and cell lines, particularly for KRAS (Figure 5C and Supplemental Figure

307    11A). Similarly, we observed a clear dose-response in MIA PaCa-2 and A427 cell lines on a

308    protein level, which showed that M2/K2 Inverted Chimera V2 substantially reduced both MYC and

309    KRAS protein levels and MAPK signaling (evaluated by ERK1/2 phosphorylation) compared to

310    individual siRNAs (Figure 5D and Supplemental Figure 11B). Using our KRAS-luciferase reporter,

311    we also observed that M2/K2 Inverted Chimera V2 was 80-fold more potent than the Kseq2 siRNA

312    alone (Figure 5E). To examine the off-target effects of our siRNAs, we conducted RNA-

313    sequencing on the A427 cells after treating with the negative control siRNA, Kseq2 Hi2OMe

314    siRNA, Mseq2 Hi2OMe siRNA, and M2/K2 Inverted Chimera V2 after 24 hrs. We found that MYC

315    and KRAS were among the top downregulated genes in their respective targeted siRNA

316    treatments, and both were strongly downregulated by the chimera (Figure 5F). Based on this data,

317    we concluded that the siRNAs are specifically targeting the genes of interest.

318

319    To evaluate the phenotypic effects of siRNA-mediated dual knockdown of MYC and KRAS, we

320    conducted a dose-response assay and found that the inverted chimeric design substantially

321    lowered the ED50 in these KRAS-dependent cell lines by >20-40 fold, going from low nM doses

322    for individual MYC or KRAS siRNAs down to as low as 100 pM for the Inverted Chimera V2 design

323    (Figure 6A). The chimeric siRNA's improved potency was also observed in small cell lung cancer

324   lines that are MYC-dependent with wild-type KRAS. As expected, KRAS siRNAs had almost no

325   inhibitory effect (Supplemental Figure 12). These results are likely due to the combined effect of

326   downregulating MYC through direct target RNA engagement and through its upstream regulator,

327   KRAS. Next, we evaluated the effects of co-targeting MYC and KRAS on spheroid formation. In

328   comparison to individual Mseq2 or Kseq2 siRNAs, the cells treated with the combination of the

329   individual siRNAs, or M2/K2 Inverted Chimera V2 showed significantly diminished spheroid

330   formation (Figure 6B). Taken together, the optimized V2 inverted chimeric siRNA demonstrates

331   marked improvements in targeting both MYC and KRAS, resulting in attenuated MAPK signaling

332   and synergistic inhibition of cancer cell viability.

333

334   **EGFR-Targeting Ligand Enables Specific Uptake Into Tumors**

335   Given the success of GalNAc-conjugated chemically optimized siRNAs (53, 59), which represent

336   the overwhelming majority of recently approved clinical siRNA therapeutics, we evaluated

337   whether a ligand-conjugated approach could target tumor cells and obviate the need for a

338   nanoparticle-based carrier. Because the epidermal growth factor receptor (EGFR) is highly

339   expressed in nearly all carcinomas and capable of receptor recycling after endocytosis (61), we

340   sought to determine whether an EGFR-targeting ligand could enable tumor-directed chimera

341   delivery. The EGFR ligand, GE11, is a 12–amino acid peptide discovered using phage-display for

342   EGFR that does not induce mitogenic signaling (62), and several independent groups have shown

343   nano-formulations of GE11 can target EGFR-expressing tumors (63, 64). Our lab has published

344   work formally evaluating whether direct linker-mediated conjugation of GE11 to oligonucleotides

345   could facilitate targeted RNAi delivery (65). Previous experiments showed that compared to

346   unconjugated siRNAs, GE11-conjugated siRNAs showed an approximate 15-fold increase in

347   uptake by EGFR-expressing cancer cells, likely due to receptor-mediated endocytosis. FACS

348   sorting on samples from a xenograft model injected subcutaneously with conjugated siRNAs

349   demonstrated robust tumor targeting, with approximately 90% of cancer cells taking up the siRNA.

350  To test the specificity of the GE11 ligand, we used an amine-based conjugation strategy to

351  covalently link GE11 with a C-terminal cysteine to a triethylene glycol (TEG) linker and the 3'-end

352  of the guide strand (66) of the MYC Hi2OMe siRNA (Figure 7A). Athymic nude mice bearing

353  subcutaneous H727 (KRAS$^{G12V}$/WT; lung carcinoid) tumors were randomly assigned to four

354  treatment groups (n=3 mice/group): 1) GE11-negative control (which is a non-targeting inert

355  siRNA), 2) GE11-Mseq2 Hi2OMe, 3) GE11-Kseq2 Hi2Ome, and 4) GE11-M2/K2 Inverted

356  Chimera V2. Once tumors reached ~75 mm$^3$, GE11-conjugated siRNAs (groups 1-3: 5 mg/kg

357  siRNA, group 4: 10 mg/kg chimera to yield 5 mg/kg of each siRNA) were injected subcutaneously

358  twice weekly. Subcutaneous injection of ligand-conjugated siRNAs has been previously shown to

359  perform better in vivo than intravenous administration (53) and is the preferred method of

360  administration clinically. Following administration, the siRNAs will diffuse slowly from the injection

361  site into the plasma, which will reach their target tissue via circulation (53). After one week of

362  treatment (or 2 doses), tumors and several somatic tissues were collected. Following RNA

363  isolation, using stem-loop RT-qPCR to detect individual guide strands, we confirmed the GE11-

364  mediated delivery platform delivered MYC and KRAS siRNAs to the tumor. Interestingly, we

365  observed a dramatic increase in the abundance of the KRAS guide strand in the MYC/KRAS

366  chimeric siRNA-treated group, suggesting the chimeric design has improved metabolic stability

367  (Figure 7B). Similar to our previously published work, we observed the presence of the guide

368  strands in other highly EGFR-expressing tissues, such as the skin and bladder (although we did

369  not observe any adverse effects in the treated mice). Due to the hydrophilic nature of the modified

370  siRNAs, clearance through the kidney was expected and observed (Figure 7C).

371

372  To evaluate for biologic effects on a protein level, we performed tumor immunohistochemistry.

373  While both KRAS and MYC siRNA-treated groups resulted in a decrease in Ki67, M2/K2 Inverted

374  Chimera V2 treatment resulted in a more significant reduction, consistent with the inhibitory

375  effects on proliferation via on-target downregulation of MYC and KRAS. Only the inverted chimeric

376  siRNA resulted in a small but significant increase in cleaved caspase-3. Consistent with potent

377  on-target regulation, treatment with MYC siRNAs resulted in a 54% reduction in MYC IHC staining

378  and MYC/KRAS inverted chimeric siRNAs resulted in a highly significant 76% reduction (Figure

379  7D). Taken together, these results demonstrate an effective, systemic EGFR-directed ligand-

380  conjugated platform for cancer delivery. Additionally, the increased metabolic stability of the

381  inverted chimeric design may further contribute to the improved effects on inhibiting proliferation

382  and MYC expression.

383

**384  Ligand-conjugated Inverted MYC/KRAS Chimeras Have Potent Anti-Tumor Activity**

385  To validate that the effect on cell viability was the result of specific gene targeting, we conducted

386  dose-response assays in several cell lines comparing all treatment groups to an additional double

387  control chimera, which links two non-targeting siRNAs in the same configuration as M2/K2

388  Inverted Chimera V2. We found that the double control chimeric siRNA had no effect on cancer

389  cell viability (Figure 8A and Supplemental Figure 13A), further confirming that the potent decrease

390  of cell viability following treatment of the MYC/KRAS inverted chimeric siRNA was due to specific

391  knockdown of the genes of interest. To test the therapeutic effects of the conjugated siRNAs on

392  tumor burden over time, Athymic nude mice bearing subcutaneous H727 tumors were randomly

393  assigned to the following treatment groups (n=10 mice/group): 1) GE11-Negative Control, 2)

394  GE11-Double Control Chimera, 3) HW12-M2/K2 Inverted Chimera V2 (which contained a non-

395  targeting version of GE11 (HW12) previously characterized by Gu et al (62)), 4) GE11-Mseq2

396  Hi2OMe, 5) GE11-Kseq2 Hi2OMe, and 6) GE11-M2/K2 Inverted Chimera V2. Once tumors

397  reached ~75 mm$^3$, mice were treated subcutaneously twice weekly (GE11-conjugated siRNA

398  groups: 5 mg/kg siRNA, GE11-conjugated chimeric siRNA groups: 10 mg/kg chimera to yield 5

399  mg/kg of each siRNA). Compared with GE11-Negative Control siRNA treatment, we observed no

400  significant tumor growth inhibition following treatment with GE11-Double Control Chimera or

401  HW12-M2/K2 Inverted Chimera V2, consistent with the chimeric structure having no efficacy on

402   its own, as well as the requirement for the GE11 ligand to achieve effective tumor delivery.

403   However, by day 7, we observed reduced tumor volumes following treatment with GE11-Mseq2

404   Hi2OMe (50%), GE11-Kseq2 Hi2OMe (30%) and the GE11-conjugated chimeric siRNA group

405   (90%) (Supplemental Figure 13B). By day 10, the groups treated with GE11-Mseq2 Hi2OMe and

406   GE11-Kseq2 Hi2OMe showed significant percent of tumor growth inhibitions (%TGIs) of 50% and

407   43%, respectively, whereas the GE11-conjugated chimeric siRNA group achieved a TGI of 66%

408   (Figure 8B). Overall, the chimeric siRNA formulation was substantially more effective at controlling

409   tumors than either KRAS- or MYC-targeting strategy alone. When repeated using the A427 lung

410   model, similar results were observed (Figure 8C and Supplemental Figure 13C). Seven days after

411   starting treatment, 100% of tumors in the GE11-conjugated chimeric siRNA group demonstrated

412   reduced tumor volumes (Figure 8D). By day 18, the GE11-conjugated chimeric siRNA group

413   achieved a TGI of 124%, whereas the groups treated with GE11-Mseq2 Hi2OMe and GE11-

414   Kseq2 Hi2OMe showed TGI's of 55% and 39%, respectively. To evaluate the pharmacodynamic

415   and pharmacokinetic properties of our ligand conjugated designs, we harvested tumors 21 days

416   after starting treatment and observed significantly diminished tumor masses in the GE11-

417   conjugated chimeric siRNA group (Figure 8E). Using stem-loop RT-qPCR to detect individual

418   guide strands, we confirmed the GE11-mediated delivery platform delivered MYC and KRAS

419   siRNAs. We observed a similar increase in the abundance of both MYC and KRAS guide strands

420   in the GE11-conjugated chimeric siRNA treated samples as previously seen in the H727 model,

421   further suggesting the chimeric design resists plasma degradation and has improved metabolic

422   stability in the target tissue (Figure 8F). Consistent with these findings, both *MYC* and *KRAS*

423   mRNA levels were significantly more downregulated in the GE11-conjugated chimeric siRNA

424   group when compared to the single siRNA treatment groups (Figure 8G).

425

426   To evaluate whether the chimeric design is an improvement over co-administration of the GE11-

427   MYC Hi2OMe and GE11-KRAS Hi2OMe individual siRNAs, we compared these treatments using

18

428    the HPAF-II (KRAS$^{G12D}$/WT) pancreatic model once tumors reached a larger size (~300 mm$^3$).

429    While mice in both treatment groups had significant tumor growth inhibition by day 7 of treatment,

430    at day 14 the relative tumor volume in the co-administered siRNA group had returned to that of

431    the control tumors. However, mice in the MYC/KRAS chimeric siRNA-treated group continued to

432    demonstrate significant tumor growth inhibition (Supplemental Figure 13D). Furthermore, 60% of

433    the mice in the MYC/KRAS chimeric siRNA treatment group survived beyond 18 days in

434    comparison to 20% of the mice in the co-administered single-targeting MYC and KRAS siRNAs

435    (Supplemental Figure 13E). This data shows the superior activity of the MYC/KRAS chimeric

436    siRNA formulation, which is likely more effective than co-administration of each single-targeting

437    siRNA due to (a) its consistent uptake and targeting of both transcripts into each tumor cell (a

438    pattern reflected in initial in vitro experiments (Figure 6B), (b) its improved potency via the

439    additional 5' dT overhangs (Figure 3C), and (c) its increased metabolic stability within the tumor

440    (Figure 7B, Figure 8F).

441

442    Clinical resistance to KRAS inhibitors is well-documented, with MAPK effector upregulation, MYC

443    amplification, and YAP/TAZ signaling emerging as key players in driving resistance (67, 68).

444    Thus, we evaluated whether the MYC/KRAS chimeric siRNA could overcome MYC amplification-

445    driven resistance to the pan-RAS inhibitor, RMC-7977 (69). Using RMC-7977 inhibitor-resistant

446    KPC cell lines, we conducted dose-response assays. Like our observations in MYC-dependent

447    small cell lung carcinoma lines (Supplemental Figure 12), KRAS silencing had no impact,

448    consistent with RAS inhibitor resistance. However, MYC siRNAs and notably MYC/KRAS

449    chimeric siRNAs significantly inhibited all 3 resistant KPC cell lines (Supplementary Figure 14A),

450    suggesting a further therapeutic advantage of deeper MYC silencing by dual KRAS and MYC

451    inhibition. To assess the preliminary efficacy and safety of this approach, we evaluated whether

452    MYC-amplification mediated resistance to pan-RAS inhibitors could be targeted in vivo. Upon

453    tumor establishment with K18399R in C57/B6J immunocompetent mice, mice were treated with

454    subcutaneous treatments of GE11-Neg Ctrl or GE11-M2/K2 Inverted Chimera V2 over three

455    weeks (6 total doses). Compared with the control group, treatment with MYC/KRAS chimeric

456    siRNAs significantly reduced tumor burden, with 6 mice showing complete tumor regression by

457    day 10; however, resistance did develop in several tumors (Supplemental Figure 14, B and C).

458    We did not observe significant changes in animal behavior, body weight, liver or kidney function.

459    Analysis on the complete cell differential also did not show any evidence of marrow toxicity or a

460    systemic inflammatory response (Supplemental Figure 14D-H).

461

462    Finally, we compared the efficacy of the MYC/KRAS chimeric siRNA with a clinically approved

463    $KRAS^{G12C}$ inhibitor (sotorasib). Using the H358 ($KRAS^{G12C}$/WT) lung adenocarcinoma model, we

464    treated mice once subcutaneous tumors reached ~200 mm$^3$ with either siRNA designs, 10 mg/kg

465    of sotorasib, or a combination of both. Similar to previous experiments, we observed in the H358

466    model that although the tumors treated with single-targeting KRAS and MYC siRNAs showed

467    disease control in comparison to the control-treated group within a week, the rate of tumor growth

468    was much more effectively inhibited following treatment with the MYC/KRAS chimeric siRNA

469    (Figure 9A, Supplemental Figure 15A). By day 18, the GE11-M2/K2 Inverted Chimera V2-treated

470    group achieved a TGI of 75%, while the groups treated with GE11-Mseq2 Hi2OMe and GE11-

471    Kseq2 Hi2OMe showed TGI's of 50% and 52%, respectively (Figure 9B). Tumors treated with

472    sotorasib achieved a TGI of 74% with no significant difference to those treated with the chimeric

473    siRNA, however, a combination treatment strategy of sotorasib and MYC/KRAS chimeric siRNA

474    administration led to highly significant responses in nearly every tumor with a peak TGI of 132%.

475    This impressive depth of response and TGI was sustained in this group through day 21 (Figure

476    9C, Supplemental Figure 15B). This data suggests that targeting KRAS and downstream effectors

477    on both a protein and mRNA level can improve tumor burden and overall survival for a more

478    extended period, highlighting a potential combination approach on targeting mutant KRAS protein

479    as well as *KRAS* and *MYC* mRNA.

480

481    Knowledge about the resistance mechanisms to KRAS inhibition is rapidly developing, however

482    resistance to dual KRAS and MYC inhibition is poorly understood. In the H358 model, while

483    tumors in the chimeric siRNA group showed significant responses to treatment (and even one

484    complete regression), many tumors eventually lost responsiveness (Figure 9D). We isolated

485    tumors from each siRNA group and probed using western blotting for known mechanisms of

486    KRAS inhibitor resistance to understand if similar pathways were responsible for driving chimeric

487    resistance. In the individual Kseq2 treatment group, KRAS protein increased (although MYC and

488    phospho-ERK expression remained relatively low), which complements previous research that

489    shows increased KRAS expression as a mechanism of resistance to KRAS inhibitors (12, 16, 70)

490    (Figure 9E). In contrast, tumors treated with the chimeric siRNA group showed maintained

491    suppression of KRAS (30% reduction) and reductions in MYC and phospho-ERK (68% reduction

492    and 98% reduction, respectively), suggesting an alternative pathway of resistance. We

493    additionally probed for phospho-YAP at serine 127, which is a marker of cytoplasmic retention of

494    YAP, and total YAP. Several published studies have shown that activation of YAP/TAZ signaling

495    can drive resistance to KRAS G12C inhibition (71, 72). We observed a significant decrease of

496    phospho-YAP$^{S127}$ in the chimeric siRNA group, indicating YAP nuclear translocation and

497    transcriptional activity. Further, we observed a significant increase in total YAP in both the

498    individual MYC siRNA group and the chimeric siRNA group. Together these findings provide

499    strong evidence that YAP signaling may be upregulated as a mechanism of resistance in

500    response to dual KRAS/MYC suppression and warrants further investigation to explore potential

501    combination therapies.

502

503

**Discussion**

Therapies in oncology such as small molecule inhibitors have resulted in remarkable improvements in survival. However, many well-characterized oncoproteins, notably MYC and ~90% of KRAS mutants, still fall into the class of "difficult to drug" targets. Additionally, despite the clinical success of $KRAS^{G12C}$ inhibitors (10, 11), numerous mechanisms of primary and adaptive resistance have emerged (12-17), leading the field to consider combinatorial strategies to maximize efficacy (73). Because mutant KRAS signaling has a pivotal role in promoting downstream MYC activation through multiple mechanisms (39, 40), the ability to co-target both oncogenes within the same cell with a single molecule represents a highly attractive drug candidate.

In this study, we developed an inverted chimeric RNAi molecule that resulted in highly potent and synergistic co-targeting of KRAS and MYC. Our results demonstrate that the guide strand of a long chimeric siRNA strand was more potent than the same guide strand delivered as a traditional single siRNA. Unexpectedly, our data support a model that this greatly enhanced potency is the result of metabolism of the chimera's thymidine bridge, which results in deoxythymidine (dT) overhangs on the 5'-end of the KRAS guide strand. While previous studies have found that 3'-dT overhangs can affect an siRNA's potency and in vivo stability (74), there are no studies to our knowledge that evaluate the effects of 5'-dT overhangs of various lengths. However, the importance of the 5' end of the guide strand is well-documented: phosphorylation of the 5' nucleoside allows for the formation of the active RISC-siRNA complex (75) and conserving the integrity of the 5' end is functionally more important than the 3' end (76). During RISC loading, low base-pairing stability on the 5' end of the guide strand characterizes siRNAs in cultured cells (77), which can also be the contributing factor for strand bias. Strategic mismatches on the 5' end can destabilize the guide strand, leading to increased retention within the Ago complex (78, 79). We posit the mechanistic basis for the observed increase in potency may be due to strand

22

530    instability introduced by a mismatched 5' 2dT overhang on the 5'-end of the guide strand, which

531    may reflect increased metabolic stability and could be an important factor in enhancing RNAi

532    activity (57). This pattern of 5'-dT overhangs may be generalized to future siRNA therapeutics

533    and should be further studied as a convenient method for increasing RNAi potency.

534

535    The modularity of the inverted chimeric siRNAs shown in this study may provide a meaningful

536    clinical advantage over traditional strategies such as small molecule inhibitors because of their

537    ability to target multiple "undruggable" genes. The thymidine bridge properties of these chimeric

538    siRNAs ensure that the individual siRNA molecules of choice are delivered to the cell in equimolar

539    proportions, another strong advantage over single-agent small molecule inhibitors which can only

540    interact with one target. Additionally, the pro-drug-like metabolic processing of these chimeric

541    molecules in acidified lysosomes leads to dramatically more potent siRNA products. We observed

542    that the MYC/KRAS chimeric siRNA combined with an approved KRAS$^{G12C}$ small molecule

543    inhibitor led to highly significant and durable reductions in tumor size, including some complete

544    regressions, suggesting that combination approaches that co-target KRAS at the mRNA and

545    protein levels may be advantageous. Additionally, we observed the MYC/KRAS chimeric siRNAs

546    can overcome resistance to pan-RAS inhibitors (RMC-7977) that occurs through MYC

547    amplifications, which may also have clinical implications.

548

549    Despite potential low receptor density and intra-tumoral heterogeneity challenges for delivering

550    ligand-conjugated siRNAs to tumors (51), our work with an EGFR-targeting moiety demonstrates

551    the capability to conjugate and deliver two linked siRNAs with a single ligand (50). The marked

552    tumor inhibition upon chimeric siRNA treatment suggests that targeting multiple oncogenic

553    pathways can greatly improve efficacy over a single-targeting agent. The chimeric siRNA showed

554    strong on-target suppression of KRAS and MYC in tumors and preliminary toxicology studies

555    indicate this modality may be safe. However, more extensive safety studies will be needed before

556    entering the clinic, notably its impact in other high EGFR-expressing tissues (such as skin and

557    the bladder) and in the kidney, which is the main site of clearance for ligand-conjugated siRNAs.

558    To demonstrate long-term safety, additional studies including dose escalation experiments for

559    establishing toxicity limits, expanded transcriptional profiling for off-target effects, and validation

560    in additional animal models will need to be performed.

561

562    Finally, our efficacy experiment in larger tumors indicate that there may be limitations to achieving

563    sufficient delivery of this RNAi molecule, which may be related to increased tumor heterogeneity,

564    disrupted vascular perfusion, or insufficient tumor loading, and should be further investigated.

565    Additionally, despite the potential increase in therapeutic window under the chimeric siRNA,

566    continued treatment does show the eventual development of resistance through YAP signaling,

567    which may be a driver of resistance under dual KRAS/MYC protein suppression. Further

568    optimization of ligand-conjugated delivery of inverted chimeras may enable improved selectivity

569    and potency of these molecules while reducing toxic side-effects. These features are attractive

570    and applicable to other complex diseases beyond cancer that may require dual targeting, such

571    as cardio-metabolic disorders, neurodegeneration, inflammation, or infectious diseases (80).

572

573

**Materials/Methods**

**Sex as a biological variant**

For murine studies, 8- to 12-week-old female athymic nude or C57/B6 mice were used. Sex was not considered as a biological variable, as the incidence and outcome of human lung and pancreatic cancers are nearly equivalent for each sex.

**siRNA transfections**

The sequences of all siRNAs are in Supplemental Table 1 and as previously described(54). All siRNA transfection experiments were completed using Lipofectamine RNAiMAX (Life Technologies) in culture media without antibiotics following manufacturer instructions.

**RT-qPCR**

Total RNA from cell lysates was purified using the Quick RNA MicroPrep Zymo Research Kit (Genesee Scientific). For mRNA analysis, cDNA was synthesized using the iScript cDNA Synthesis Kit (Bio-Rad) as per the manufacturer's instructions. Analysis of RNA levels was determined by a StepOnePlus Real-Time PCR System (Applied Biosystems) using SYBR Green Master Mix (Bio-Rad). A list of gene-specific primers used for RT-qPCR is included in Supplemental Table 3. Reactions were run in duplicate or triplicate. Fold change was calculated using the $2^{-\Delta\Delta CT}$ method and experiments were normalized to expression of the rRNA 18S and expression of target genes in the negative control-treated samples. Graphs were generated with GraphPad Prism (GraphPad).

**Cell viability experiments**

Cell viability in response to siRNA treatment was evaluated with the CellTiter-Glo 2.0 Cell Viability Assay using the manufacturer's protocol (Promega). Resuspended MIA PaCa-2 cells in culture

600  media were seeded at 1,000 cells/well and resuspended A427 cells were seeded at 3,500

601  cells/well in opaque, flat bottom 96-well plates. All cells were counted with the Countess 3

602  Automated Cell Counter (ThermoFisher). All siRNAs (suspended in serum-free media with

603  Lipofectamine RNAiMAX) were tested in triplicate starting at 40 or 20nM and progressing through

604  a 10-point serial dilution. Plates were incubated in culture conditions for 5-6 days. For viability

605  readouts, 120 µls of media was removed from each well and an equal volume of CellTiter Glo 2.0

606  (CTG) Reagent was added. Luminescence was measured at 530 nm excitation and 590 nm

607  emission on a Synergy2 fluorescent plate reader (BioTek). Data was analyzed in GraphPad

608  Prism. Experiments were repeated at least three times and representative dose-response curves

609  are shown in the figures for this paper.

610

611  **Luciferase experiments**

612  Changes in KRAS-Firefly luciferase expression in response to siRNA treatment were evaluated

613  with the Luc-Pair™ Duo-Luciferase HT Assay Kit using the manufacturer's protocol

614  (Genecopoeia). Resuspended cells in culture media were added to opaque, flat bottom 96-well

615  plates. A-431 KRAS-luciferase cells were seeded at 3,500 cells/well and were counted with the

616  Countess 3 Automated Cell Counter (ThermoFisher). All siRNAs (suspended in serum-free media

617  with Lipofectamine RNAiMAX) were tested in triplicate starting at 40 or 20nM and progressing

618  through a 10-point serial dilution. Plates were incubated in culture conditions for 3-4 days. For

619  luciferase readouts, 120 µls of media was removed from each well and an equal volume of

620  working Fluc reagent was added and incubated for ten minutes. Luminescence was measured at

621  530 nm excitation and 590 nm emission on a Synergy2 fluorescent plate reader (BioTek). An

622  equal volume of working Rluc reagent was subsequently added and incubated for an additional

623  five minutes, and luminescence was measured as above. The ratio of luminescence from the

624  Firefly luciferase to the Renilla luciferase was then calculated. Data was analyzed in GraphPad

625    Prism and ED50 curves were produced. Relative potency was calculated by dividing the ED50

626    value of the Kseq2 Hi2Ome-treated cells with the ED50 value of the other conditions.

627

628    **3D spheroid formation assay**

629    A427 and MIA PaCa-2 cells were seeded into 12-well plates and treated with 5, 10, or 20nM of

630    siRNAs and Lipofectamine RNAiMax in culture media without antibiotic for 24 hours. Cells were

631    then lifted with Trypsin and counted. 5,000 cells from each condition were mixed with 50 µls of

632    cold Matrigel (Corning) and plated onto 24-well glass bottom plates. After solidification of the

633    matrix, complete media with 10% FBS and antibiotic was added to every well. Plates were

634    incubated for 4-5 days and then imaged with a Leica Dmi8 inverted microscope (5x objective).

635    Spheroid area and number in each condition were quantified using the Organoseg software(81).

636    Graphs were generated using GraphPad Prism.

637

638    **In vivo modeling and tissue processing**

639    Animals were cared for according to guidelines set forth by the American Association for

640    Accreditation of Laboratory Animal Care and the U.S. Public Health Service policy on Human

641    Care and Use of Laboratory Animals. Mouse studies were approved and supervised by the

642    University of North Carolina at Chapel Hill Institutional Animal Care and Use Committee. Athymic

643    nude mice or C57/B6 mice were between 8-12 weeks of age at the time of injection. Cells were

644    trypsinized, washed and resuspended in Hanks balanced salt solution (HBSS; Gibco), and

645    $3.5 \times 10^6$ of A427, H358, H727, or HPAF-II cells or $5 \times 10^5$ of K18399R cells were injected

646    subcutaneously in a 50 µLs 1:1 mixture of HBSS and BD Matrigel (BD Biosciences). Caliper

647    measurements of subcutaneous tumor growth were taken twice weekly (unless otherwise

648    indicated), and tumor volume was calculated as $L \times W^2$ where L is the greatest cross-sectional

649    length across the tumor and W is the length perpendicular to L. Once tumors reached ~75-300

650    $mm^3$ in volume, mice were randomly assigned to treatment groups and injected subcutaneously

651 twice weekly at either 5 mg/kg for a single-targeting siRNA, 10 mg/kg (thus 5 mg/kg of each

652 siRNA) for the chimeras, or 10 mg/kg of sotorasib. Peptides were synthesized by the Chemical

653 Products Corporation (CPC) and sent to Avecia or Synoligo for conjugation to modified siRNAs.

654 Sotorasib (AMG510) was purchased from Medkoo (CAS#: 2252403-46-6). Tumor weights and

655 blood were obtained following necropsy, and tumors were snap frozen or fixed in 10% formalin

656 prior to downstream analyses.

657

658 **Statistical analysis for experimental data**

659 Results for each group were compared using unpaired one-tailed Student's t-test corrected for

660 multiple comparisons using the Bonferroni method, Mann-Whitney test corrected for multiple

661 comparisons using the Bonferroni method (if the data did not have a Gaussian distribution), one-

662 tailed analysis of variance (ANOVA), or Fisher's exact test (for contingency analysis). For survival

663 studies, Log-rank (Mantel-Cox) test was used. A p-value less than 0.05 was deemed statistically

664 significant unless otherwise stated in the figure legend. All statistical tests for in vitro and in vivo

665 experiments were performed using GraphPad Prism 7 (GraphPad Software, Inc., San Diego, CA).

666

667 **Study approval**

668 Mouse studies were approved and supervised by the University of North Carolina at Chapel Hill

669 Institutional Animal Care and Use Committee.

670

671 **Availability of materials**

672 All data generated or analyzed during this study (including values for all data points) are included

673 in this published article (and its supplemental information and data points files). Sequencing data

674 can be accessed with GEO accession number: GSE261735 (enter token cvqrsqawljundkz). Any

675 unique biological materials are available upon request.

676

677 **Authors' contributions**

678 YSC, AAB, ME, and CVP were involved in conceptualization of the project and relevant aims. AP

679 was involved in data curation and software implementation for large data sets (including RNAseq

680 data). YSC, HPH, SSS, LJS, CGF, KW, LE, SA, MCF, JI, AP, JLP and IS were involved in formal

681 analysis, investigation, methodology, validation, and visualization for the data included in the

682 manuscript. CVP is the primary project administrator and acquired funding for the project. All

683 authors read, edited, and approved the final manuscript.

684

685 **Acknowledgments**

696

697

698

699

700

701

702                                    References
703

704    1.    Mustachio LM, Chelariu-Raicu A, Szekvolgyi L, and Roszik J. Targeting KRAS in Cancer:

705        Promising Therapeutic Strategies. *Cancers (Basel).* 2021;13(6).

706    2.    Friday BB, and Adjei AA. K-ras as a target for cancer therapy. *Biochim Biophys Acta.*

707        2005;1756(2):127-44.

708    3.    Waters AM, and Der CJ. KRAS: The Critical Driver and Therapeutic Target for Pancreatic

709        Cancer. *Cold Spring Harb Perspect Med.* 2018;8(9).

710    4.    Dang CV, Reddy EP, Shokat KM, and Soucek L. Drugging the 'undruggable' cancer

711        targets. *Nat Rev Cancer.* 2017;17(8):502-8.

712    5.    Verdine GL, and Walensky LD. The challenge of drugging undruggable targets in cancer:

713        lessons learned from targeting BCL-2 family members. *Clin Cancer Res.*

714        2007;13(24):7264-70.

715    6.    Ostrem JM, Peters U, Sos ML, Wells JA, and Shokat KM. K-Ras(G12C) inhibitors

716        allosterically control GTP affinity and effector interactions. *Nature.* 2013;503(7477):548-

717        51.

718    7.    Hallin J, Engstrom LD, Hargis L, Calinisan A, Aranda R, Briere DM, et al. The

719        KRAS(G12C) Inhibitor MRTX849 Provides Insight toward Therapeutic Susceptibility of

720        KRAS-Mutant Cancers in Mouse Models and Patients. *Cancer Discov.* 2020;10(1):54-71.

721    8.    Canon J, Rex K, Saiki AY, Mohr C, Cooke K, Bagal D, et al. The clinical KRAS(G12C)

722        inhibitor AMG 510 drives anti-tumour immunity. *Nature.* 2019;575(7781):217-23.

723    9.    Hong DS, Fakih MG, Strickler JH, Desai J, Durm GA, Shapiro GI, et al. KRAS(G12C)

724        Inhibition with Sotorasib in Advanced Solid Tumors. *N Engl J Med.* 2020;383(13):1207-

725        17.

726    10.    Janne PA, Riely GJ, Gadgeel SM, Heist RS, Ou SI, Pacheco JM, et al. Adagrasib in Non-

727        Small-Cell Lung Cancer Harboring a KRAS(G12C) Mutation. *The New England journal of*

728        *medicine.* 2022;387(2):120-31.

729    11.    Skoulidis F, Li BT, Dy GK, Price TJ, Falchook GS, Wolf J, et al. Sotorasib for Lung Cancers

730          with KRAS p.G12C Mutation. *N Engl J Med.* 2021;384(25):2371-81.

731    12.    Awad MM, Liu S, Rybkin, II, Arbour KC, Dilly J, Zhu VW, et al. Acquired Resistance to

732          KRAS(G12C) Inhibition in Cancer. *N Engl J Med.* 2021;384(25):2382-93.

733    13.    Tanaka N, Lin JJ, Li C, Ryan MB, Zhang J, Kiedrowski LA, et al. Clinical acquired

734          resistance to KRASG12C inhibition through a novel KRAS switch-II pocket mutation and

735          polyclonal alterations converging on RAS-MAPK reactivation. *Cancer discovery.* 2021.

736    14.    Tsai YS, Woodcock MG, Azam SH, Thorne LB, Kanchi KL, Parker JS, et al. Rapid

737          idiosyncratic mechanisms of clinical resistance to KRAS G12C inhibition. *J Clin Invest.*

738          2022;132(4).

739    15.    Xue JY, Zhao Y, Aronowitz J, Mai TT, Vides A, Qeriqi B, et al. Rapid non-uniform

740          adaptation to conformation-specific KRAS(G12C) inhibition. *Nature.* 2020;577(7790):421-

741          5.

742    16.    Zhao Y, Murciano-Goroff YR, Xue JY, Ang A, Lucas J, Mai TT, et al. Diverse alterations

743          associated with resistance to KRAS(G12C) inhibition. *Nature.* 2021;599(7886):679-83.

744    17.    Akhave NS, Biter AB, and Hong DS. Mechanisms of Resistance to KRAS(G12C)-Targeted

745          Therapy. *Cancer discovery.* 2021.

746    18.    Uras IZ, Moll HP, and Casanova E. Targeting KRAS Mutant Non-Small-Cell Lung Cancer:

747          Past, Present and Future. *Int J Mol Sci.* 2020;21(12).

748    19.    Schirripa M, Nappo F, Cremolini C, Salvatore L, Rossini D, Bensi M, et al. KRAS G12C

749          Metastatic Colorectal Cancer: Specific Features of a New Emerging Target Population.

750          *Clin Colorectal Cancer.* 2020;19(3):219-25.

751    20.    Mahauad-Fernandez WD, and Felsher DW. The Myc and Ras Partnership in Cancer:

752          Indistinguishable Alliance or Contextual Relationship? *Cancer Res.* 2020;80(18):3799-

753          802.

754    21.    Kerkhoff E, Houben R, Loffler S, Troppmair J, Lee JE, and Rapp UR. Regulation of c-myc
755          expression by Ras/Raf signalling. *Oncogene.* 1998;16(2):211-6.

756    22.    Kortlever RM, Sodir NM, Wilson CH, Burkhart DL, Pellegrinet L, Brown Swigart L, et al.
757          Myc Cooperates with Ras by Programming Inflammation and Immune Suppression. *Cell.*
758          2017;171(6):1301-15 e14.

759    23.    Macaya I, Roman M, Welch C, Entrialgo-Cadierno R, Salmon M, Santos A, et al.
760          Signature-driven repurposing of Midostaurin for combination with MEK1/2 and
761          KRASG12C inhibitors in lung cancer. *Nat Commun.* 2023;14(1):6332.

762    24.    Wang Y, Yao M, Li C, Yang K, Qin X, Xu L, et al. Targeting ST8SIA6-AS1 counteracts
763          KRAS(G12C) inhibitor resistance through abolishing the reciprocal activation of PLK1/c-
764          Myc signaling. *Exp Hematol Oncol.* 2023;12(1):105.

765    25.    Silvis MR, Silva D, Rohweder R, Schuman S, Gudipaty S, Truong A, et al. MYC-mediated
766          resistance to trametinib and HCQ in PDAC is overcome by CDK4/6 and lysosomal
767          inhibition. *J Exp Med.* 2023;220(3).

768    26.    Dang CV. MYC on the path to cancer. *Cell.* 2012;149(1):22-35.

769    27.    Jain M, Arvanitis C, Chu K, Dewey W, Leonhardt E, Trinh M, et al. Sustained loss of a
770          neoplastic phenotype by brief inactivation of MYC. *Science.* 2002;297(5578):102-4.

771    28.    Soucek L, Helmer-Citterich M, Sacco A, Jucker R, Cesareni G, and Nasi S. Design and
772          properties of a Myc derivative that efficiently homodimerizes. *Oncogene.*
773          1998;17(19):2463-72.

774    29.    Gabay M, Li Y, and Felsher DW. MYC activation is a hallmark of cancer initiation and
775          maintenance. *Cold Spring Harb Perspect Med.* 2014;4(6).

776    30.    Soucek L, Whitfield J, Martins CP, Finch AJ, Murphy DJ, Sodir NM, et al. Modelling Myc
777          inhibition as a cancer therapy. *Nature.* 2008;455(7213):679-83.

778    31.    Chen H, Liu H, and Qing G. Targeting oncogenic Myc as a strategy for cancer treatment.
779          *Signal Transduct Target Ther.* 2018;3:5.

780    32.    Wang C, Zhang J, Yin J, Gan Y, Xu S, Gu Y, et al. Alternative approaches to target Myc
781        for cancer treatment. *Signal Transduct Target Ther.* 2021;6(1):117.

782    33.    Carabet LA, Rennie PS, and Cherkasov A. Therapeutic Inhibition of Myc in Cancer.
783        Structural Bases and Computer-Aided Drug Discovery Approaches. *Int J Mol Sci.*
784        2018;20(1).

785    34.    Soucek L, Whitfield JR, Sodir NM, Masso-Valles D, Serrano E, Karnezis AN, et al.
786        Inhibition of Myc family proteins eradicates KRas-driven lung cancer in mice. *Genes Dev.*
787        2013;27(5):504-13.

788    35.    Han H, Jain AD, Truica MI, Izquierdo-Ferrer J, Anker JF, Lysy B, et al. Small-Molecule
789        MYC Inhibitors Suppress Tumor Growth and Enhance Immunotherapy. *Cancer Cell.*
790        2019;36(5):483-97 e15.

791    36.    Habib S, Ariatti M, and Singh M. Anti-c-myc RNAi-Based Onconanotherapeutics.
792        *Biomedicines.* 2020;8(12).

793    37.    Miller AJ, Chang A, and Cunningham PN. Chronic Microangiopathy Due to DCR-MYC, a
794        Myc-Targeted Short Interfering RNA. *Am J Kidney Dis.* 2020;75(4):513-6.

795    38.    Whitfield JR, and Soucek L. The long journey to bring a Myc inhibitor to the clinic. *J Cell*
796        *Biol.* 2021;220(8).

797    39.    Sears R, Nuckolls F, Haura E, Taya Y, Tamai K, and Nevins JR. Multiple Ras-dependent
798        phosphorylation pathways regulate Myc protein stability. *Genes Dev.* 2000;14(19):2501-
799        14.

800    40.    Vaseva AV, Blake DR, Gilbert TSK, Ng S, Hostetter G, Azam SH, et al. KRAS
801        Suppression-Induced Degradation of MYC Is Antagonized by a MEK5-ERK5
802        Compensatory Mechanism. *Cancer Cell.* 2018;34(5):807-22 e7.

803    41.    Ischenko I, Zhi J, Hayman MJ, and Petrenko O. KRAS-dependent suppression of MYC
804        enhances the sensitivity of cancer cells to cytotoxic agents. *Oncotarget.*
805        2017;8(11):17995-8009.

806     42.     Podsypanina K, Politi K, Beverly LJ, and Varmus HE. Oncogene cooperation in tumor
807         maintenance and tumor recurrence in mouse mammary tumors induced by Myc and
808         mutant Kras. *Proc Natl Acad Sci U S A.* 2008;105(13):5242-7.

809     43.     Tran PT, Fan AC, Bendapudi PK, Koh S, Komatsubara K, Chen J, et al. Combined
810         Inactivation of MYC and K-Ras oncogenes reverses tumorigenesis in lung
811         adenocarcinomas and lymphomas. *PLoS One.* 2008;3(5):e2125.

812     44.     Pecot CV, Calin GA, Coleman RL, Lopez-Berestein G, and Sood AK. RNA interference in
813         the clinic: challenges and future directions. *Nat Rev Cancer.* 2011;11(1):59-67.

814     45.     Egli M, and Manoharan M. Re-Engineering RNA Molecules into Therapeutic Agents. *Acc
815         Chem Res.* 2019;52(4):1036-47.

816     46.     Adams D, Gonzalez-Duarte A, O'Riordan WD, Yang CC, Ueda M, Kristen AV, et al.
817         Patisiran, an RNAi Therapeutic, for Hereditary Transthyretin Amyloidosis. *The New
818         England journal of medicine.* 2018;379(1):11-21.

819     47.     Ray KK, Wright RS, Kallend D, Koenig W, Leiter LA, Raal FJ, et al. Two Phase 3 Trials of
820         Inclisiran in Patients with Elevated LDL Cholesterol. *The New England journal of medicine.*
821         2020;382(16):1507-19.

822     48.     Sardh E, Harper P, Balwani M, Stein P, Rees D, Bissell DM, et al. Phase 1 Trial of an RNA
823         Interference Therapy for Acute Intermittent Porphyria. *The New England journal of
824         medicine.* 2019;380(6):549-58.

825     49.     Wong SC, Cheng W, Hamilton H, Nicholas AL, Wakefield DH, Almeida A, et al. HIF2alpha-
826         Targeted RNAi Therapeutic Inhibits Clear Cell Renal Cell Carcinoma. *Molecular cancer
827         therapeutics.* 2018;17(1):140-9.

828     50.     Klein D, Goldberg S, Theile CS, Dambra R, Haskell K, Kuhar E, et al. Centyrin ligands for
829         extrahepatic delivery of siRNA. *Molecular therapy : the journal of the American Society of
830         Gene Therapy.* 2021.

831  51.  Abdelaal AM, and Kasinski AL. Ligand-mediated delivery of RNAi-based therapeutics for
832       the treatment of oncological diseases. *NAR Cancer.* 2021;3(3):zcab030.

833  52.  Khvorova A, and Watts JK. The chemical evolution of oligonucleotide therapies of clinical
834       utility. *Nat Biotechnol.* 2017;35(3):238-48.

835  53.  Nair JK, Willoughby JL, Chan A, Charisse K, Alam MR, Wang Q, et al. Multivalent N-
836       acetylgalactosamine-conjugated siRNA localizes in hepatocytes and elicits robust RNAi-
837       mediated gene silencing. *J Am Chem Soc.* 2014;136(49):16958-61.

838  54.  Pecot CV, Wu SY, Bellister S, Filant J, Rupaimoole R, Hisamatsu T, et al. Therapeutic
839       silencing of KRAS using systemically delivered siRNAs. *Molecular cancer therapeutics.*
840       2014;13(12):2876-85.

841  55.  Brown CR, Gupta S, Qin J, Racie T, He G, Lentini S, et al. Investigating the
842       pharmacodynamic durability of GalNAc-siRNA conjugates. *Nucleic Acids Res.*
843       2020;48(21):11827-44.

844  56.  Subramanian RR, Wysk MA, Ogilvie KM, Bhat A, Kuang B, Rockel TD, et al. Enhancing
845       antisense efficacy with multimers and multi-targeting oligonucleotides (MTOs) using
846       cleavable linkers. *Nucleic Acids Res.* 2015;43(19):9123-32.

847  57.  Nair JK, Attarwala H, Sehgal A, Wang Q, Aluri K, Zhang X, et al. Impact of enhanced
848       metabolic stability on pharmacokinetics and pharmacodynamics of GalNAc-siRNA
849       conjugates. *Nucleic Acids Res.* 2017;45(19):10969-77.

850  58.  Dominska M, and Dykxhoorn DM. Breaking down the barriers: siRNA delivery and
851       endosome escape. *J Cell Sci.* 2010;123(Pt 8):1183-9.

852  59.  Foster DJ, Brown CR, Shaikh S, Trapp C, Schlegel MK, Qian K, et al. Advanced siRNA
853       Designs Further Improve In Vivo Performance of GalNAc-siRNA Conjugates. *Mol Ther.*
854       2018;26(3):708-17.

855   60.   Papke B, Azam SH, Feng AY, Gutierrez-Ford C, Huggins H, Pallan PS, et al. Silencing of
856         Oncogenic KRAS by Mutant-Selective Small Interfering RNA. *ACS Pharmacol Transl Sci.*
857         2021;4(2):703-12.

858   61.   Sorkin A, and Duex JE. Quantitative analysis of endocytosis and turnover of epidermal
859         growth factor (EGF) and EGF receptor. *Curr Protoc Cell Biol.* 2010;Chapter 15:Unit 15 4.

860   62.   Li Z, Zhao R, Wu X, Sun Y, Yao M, Li J, et al. Identification and characterization of a novel
861         peptide ligand of epidermal growth factor receptor for targeted delivery of therapeutics.
862         *FASEB J.* 2005;19(14):1978-85.

863   63.   Genta I, Chiesa E, Colzani B, Modena T, Conti B, and Dorati R. GE11 Peptide as an Active
864         Targeting Agent in Antitumor Therapy: A Minireview. *Pharmaceutics.* 2017;10(1).

865   64.   Alexander-Bryant AA, Zhang H, Attaway CC, Pugh W, Eggart L, Sansevere RM, et al.
866         Dual peptide-mediated targeted delivery of bioactive siRNAs to oral cancer cells in vivo.
867         *Oral Oncol.* 2017;72:123-31.

868   65.   Stanland LJ, Huggins HP, Sahoo SS, Porrello A, Chareddy Y, Azam SH, et al. A first-in-
869         class EGFR-directed KRAS G12V selective inhibitor. *Cancer Cell.* 2025.

870   66.   Weingartner A, Bethge L, Weiss L, Sternberger M, and Lindholm MW. Less Is More: Novel
871         Hepatocyte-Targeted siRNA Conjugates for Treatment of Liver-Related Disorders. *Mol*
872         *Ther Nucleic Acids.* 2020;21:242-50.

873   67.   Dilly J, Hoffman MT, Abbassi L, Li Z, Paradiso F, Parent BD, et al. Mechanisms of
874         Resistance to Oncogenic KRAS Inhibition in Pancreatic Cancer. *Cancer Discov.*
875         2024;14(11):2135-61.

876   68.   Isermann T, Sers C, Der CJ, and Papke B. KRAS inhibitors: resistance drivers and
877         combinatorial strategies. *Trends Cancer.* 2025;11(2):91-116.

878   69.   Wasko UN, Jiang J, Dalton TC, Curiel-Garcia A, Edwards AC, Wang Y, et al. Tumour-
879         selective activity of RAS-GTP inhibition in pancreatic cancer. *Nature.*
880         2024;629(8013):927-36.

881    70.    Yaeger R, Mezzadra R, Sinopoli J, Bian Y, Marasco M, Kaplun E, et al. Molecular
882           Characterization of Acquired Resistance to KRASG12C-EGFR Inhibition in Colorectal
883           Cancer. *Cancer Discov.* 2023;13(1):41-55.

884    71.    Edwards AC, Stalnecker CA, Jean Morales A, Taylor KE, Klomp JE, Klomp JA, et al. TEAD
885           Inhibition Overcomes YAP1/TAZ-Driven Primary and Acquired Resistance to KRASG12C
886           Inhibitors. *Cancer Res.* 2023;83(24):4112-29.

887    72.    Hagenbeek TJ, Zbieg JR, Hafner M, Mroue R, Lacap JA, Sodir NM, et al. An allosteric
888           pan-TEAD inhibitor blocks oncogenic YAP/TAZ signaling and overcomes KRAS G12C
889           inhibitor resistance. *Nat Cancer.* 2023;4(6):812-28.

890    73.    Hofmann MH, Gerlach D, Misale S, Petronczki M, and Kraut N. Expanding the Reach of
891           Precision Oncology by Drugging All KRAS Mutants. *Cancer discovery.* 2022.

892    74.    Strapps WR, Pickering V, Muiru GT, Rice J, Orsborn S, Polisky BA, et al. The siRNA
893           sequence and guide strand overhangs are determinants of in vivo duration of silencing.
894           *Nucleic Acids Res.* 2010;38(14):4788-97.

895    75.    Chiu YL, and Rana TM. RNAi in human cells: basic structural and functional features of
896           small interfering RNA. *Mol Cell.* 2002;10(3):549-61.

897    76.    Chiu YL, and Rana TM. siRNA function in RNAi: a chemical modification analysis. *RNA.*
898           2003;9(9):1034-48.

899    77.    Khvorova A, Reynolds A, and Jayasena SD. Functional siRNAs and miRNAs exhibit
900           strand bias. *Cell.* 2003;115(2):209-16.

901    78.    Schwarz DS, Hutvagner G, Du T, Xu Z, Aronin N, and Zamore PD. Asymmetry in the
902           assembly of the RNAi enzyme complex. *Cell.* 2003;115(2):199-208.

903    79.    Lisowiec-Wachnicka J, Bartys N, and Pasternak A. A systematic study on the influence of
904           thermodynamic asymmetry of 5'-ends of siRNA duplexes in relation to their silencing
905           potency. *Sci Rep.* 2019;9(1):2477.

906    80.    Ramsay RR, Popovic-Nikolic MR, Nikolic K, Uliassi E, and Bolognesi ML. A perspective

907           on multi-target drug discovery and design for complex diseases. *Clin Transl Med.*

908           2018;7(1):3.

909    81.    Borten MA, Bajikar SS, Sasaki N, Clevers H, and Janes KA. Automated brightfield

910           morphometry of 3D organoid populations by OrganoSeg. *Sci Rep.* 2018;8(1):5319.
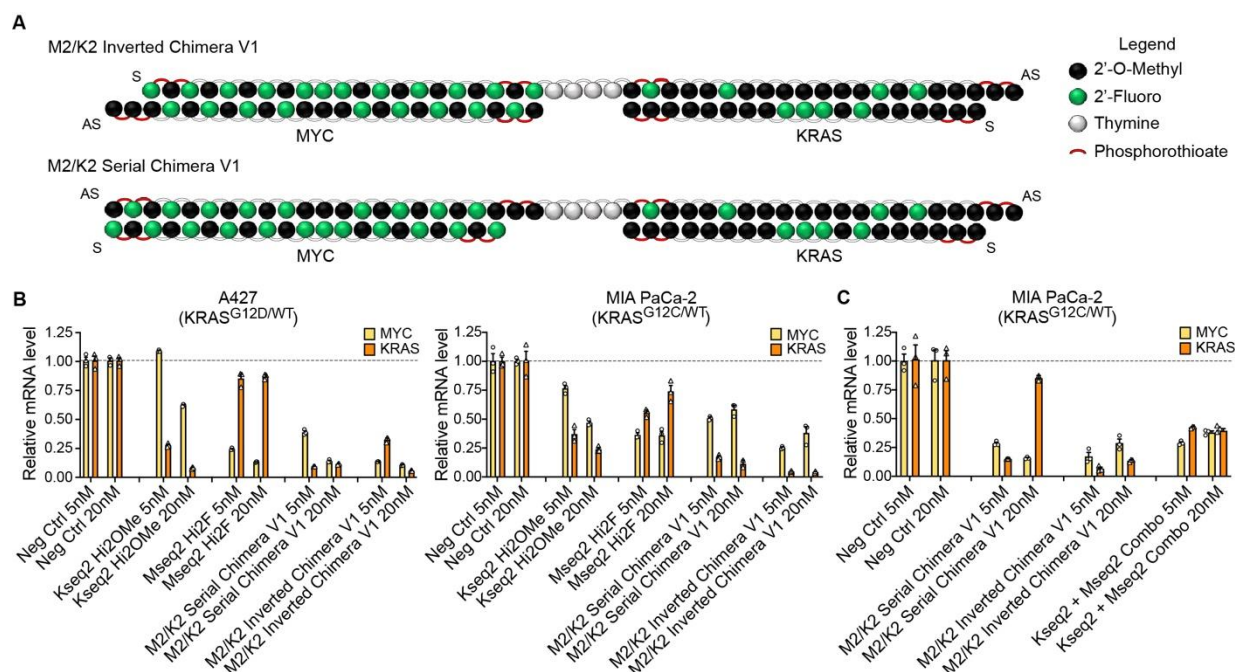
911
912

913

914

**Figure 1. Design and in vitro activity of MYC/KRAS chimeric siRNAs.** (**A**) Structures of the inverted and serial conformations of a MYC/KRAS co-targeting chimeric siRNA. In the inverted conformation (M2/K2 Inverted Chimera V1), the MYC siRNA passenger (sense, S) strand is linked via a d(T)$_4$ bridge to the KRAS siRNA guide (antisense, AS) strand. In the serial conformation (M2/K2 Serial Chimera V1), the MYC siRNA guide (antisense, AS) strand is linked via a d(T)$_4$ bridge to the KRAS siRNA guide (antisense, AS) strand. (**B-C**) Relative *MYC* and *KRAS* mRNA expression by RT-qPCR after siRNA treatment at 5 and 20nM for 48-72 hrs in A427 and MIA PaCa-2 cells. In conditions with MYC + KRAS co-transfection, each of the MYC and KRAS siRNAs were transfected at the indicated dose. Data are shown as the mean ± SEM.

924

925
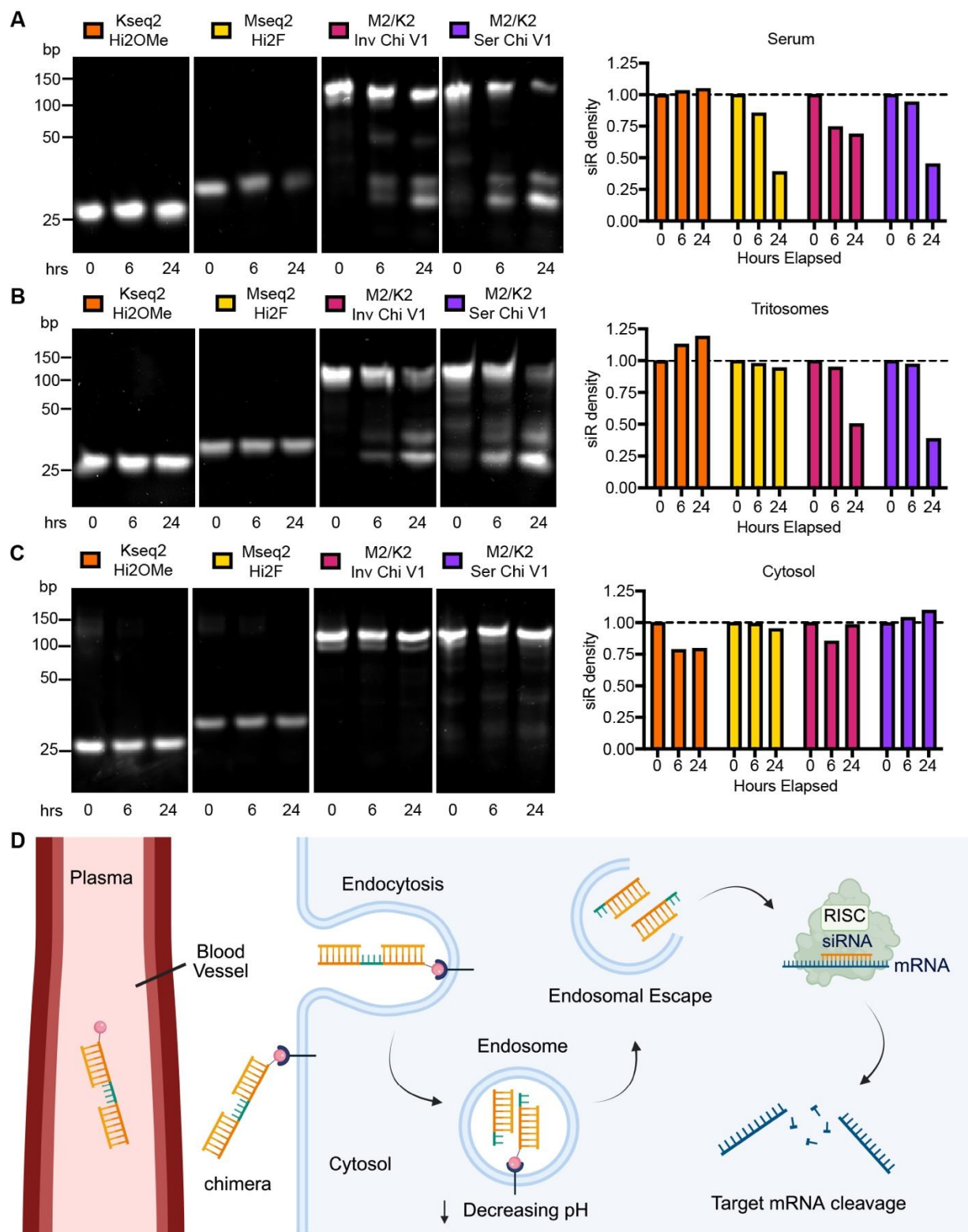
**Figure 2. Stability of MYC/KRAS chimeric siRNAs in different cellular conditions.** (**A**)

Evaluation of siRNA stability in serum. 10μM of the MYC Hi2F, KRAS Hi2OMe, M2/K2 Inverted

929    Chimera V1 (M2/K2 Inv Chi V1), and M2/K2 Serial Chimera V1 (M2/K2 Ser Chi V1) siRNAs were

930    incubated in 50% FBS for 0, 6, and 24 hrs. (**B**) Evaluation of siRNA stability in tritosomes. 4µM of

931    the MYC Hi2F, KRAS Hi2OMe, M2/K2 Inv Chi V1, and M2/K2 Ser Chi V1 siRNAs were incubated

932    in acidified rat liver tritosomes for 0, 6, and 24 hrs. (**C**) Evaluation of siRNA stability in cytosol.

933    10µM of the MYC Hi2F, KRAS Hi2OMe, , M2/K2 Inv Chi V1, and M2/K2 Ser Chi V1 siRNAs were

934    incubated in rat liver cytosol for 0, 6, and 24 hrs. (**A-C**) Quantification of relative band intensities

935    included to the right, which were normalized to the 0 hr timepoint for each siRNA. Images are

936    representative of experiments conducted two times. (**D**) Schematic of siRNA metabolism following

937    in vivo administration. Created with Biorender.com.

938

939

**A** Expression of KRAS-Luciferase

**B** M2/K2 Inverted Chimera V2 (PS bridge)

Kseq2 1dT

Kseq2 2dT

Kseq2 3dT

Kseq2 4dT

Legend
- 2'-O-Methyl
- 2'-Fluoro
- Thymine
- Phosphorothioate

**C** Expression of KRAS-Luciferase

940
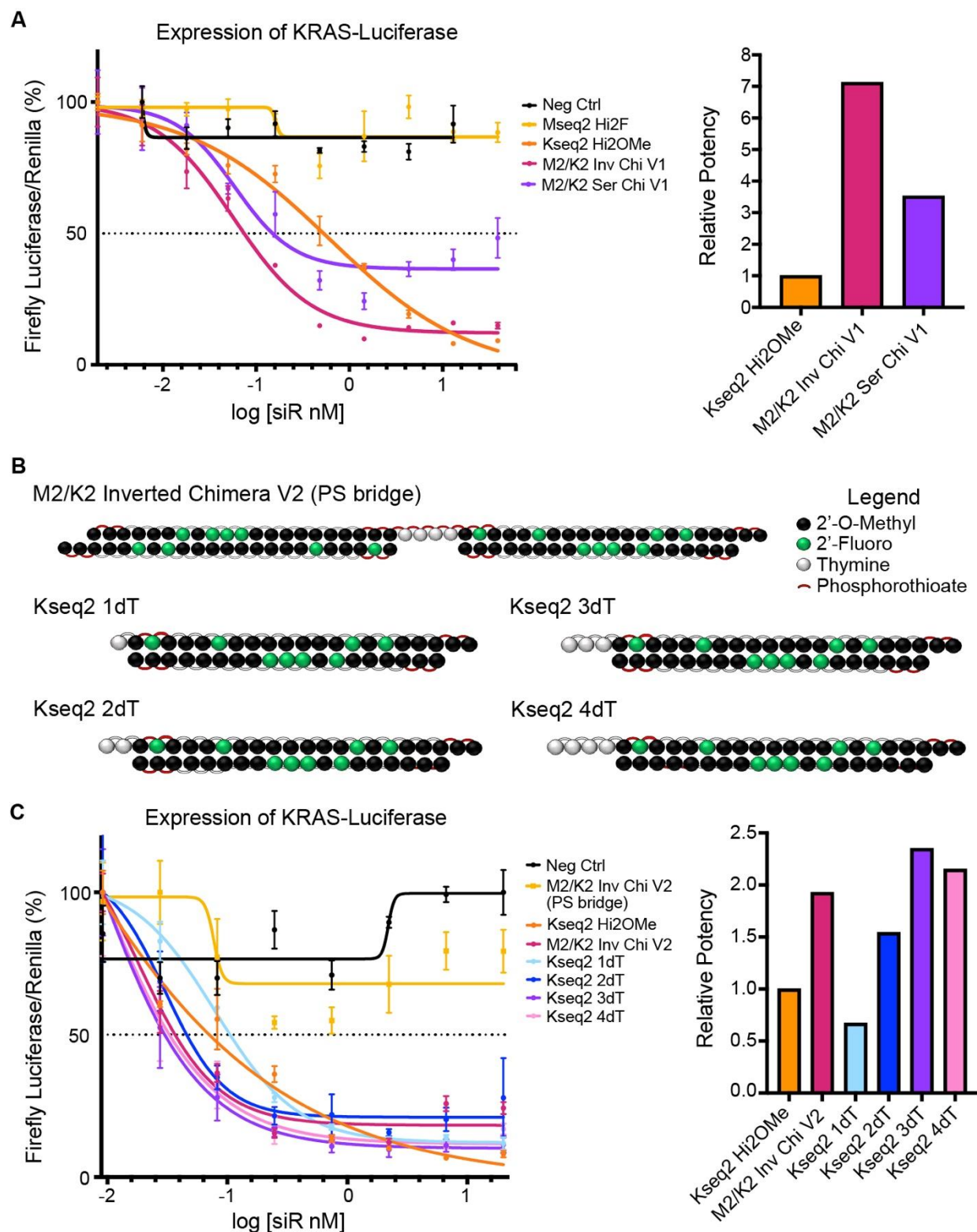
941 **Figure 3. Characterization of MYC/KRAS chimeric siRNA mechanism of action. (A)** Dose-

942 response curves (left) and relative ED50s (right, calculated as ED50 of siRNA divided by the

943    ED50 of Kseq2 Hi2OMe) of KRAS-Firefly luciferase expression in A-431 KRAS-knockout cells

944    treated with the negative control (NC) siRNA, MYC Hi2F, KRAS Hi2OMe, M2/K2 Inverted

945    Chimera V1 (M2/K2 Inv Chi V1), and M2/K2 Serial Chimera V1 (M2/K2 Ser Chi V1). All Firefly-

946    luciferase luminescence values were normalized with Renilla-luciferase luminescence and

947    expressed as a percentage. Data are representative of three replicates and error bars represent

948    SEM. (**B**) Structures of M2/K2 Inverted Chimera V2 with a fully phosphorothioate-modified bridge

949    that renders it uncleavable, and the four possible iterations of the metabolized Kseq2 siRNA with

950    1, 2, 3, or 4 dT overhangs. (**C**) Dose-response curves (left) and relative ED50s (right, calculated

951    as ED50 of siRNA divided by the ED50 of Kseq2 Hi2OMe) of KRAS-Firefly luciferase expression

952    in A-431 KRAS-knockout cells treated with the NC siRNA, M2/K2 Inverted Chimera V2 with a fully

953    phosphorothioate-modified thymidine bridge (M2/K2 Inv Chi V2 (PS bridge)), KRAS Hi2OMe,

954    M2/K2 Inverted Chimera V2 (M2/K2 Inv Chi V2), Kseq2 1dT, Kseq2 2dT, Kseq2 3dT, and Kseq2

955    4dT. All Firefly-luciferase luminescence values were normalized with Renilla-luciferase

956    luminescence and expressed as a percentage. Data are representative of two replicates and error
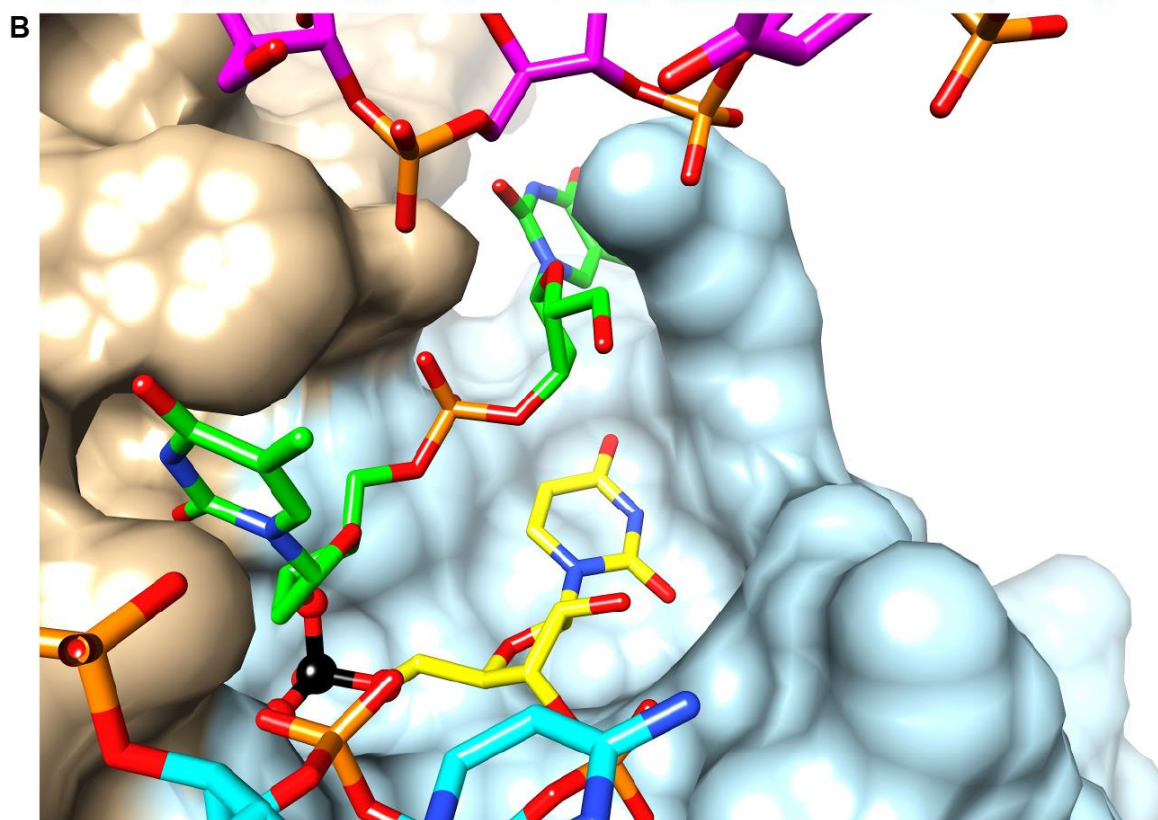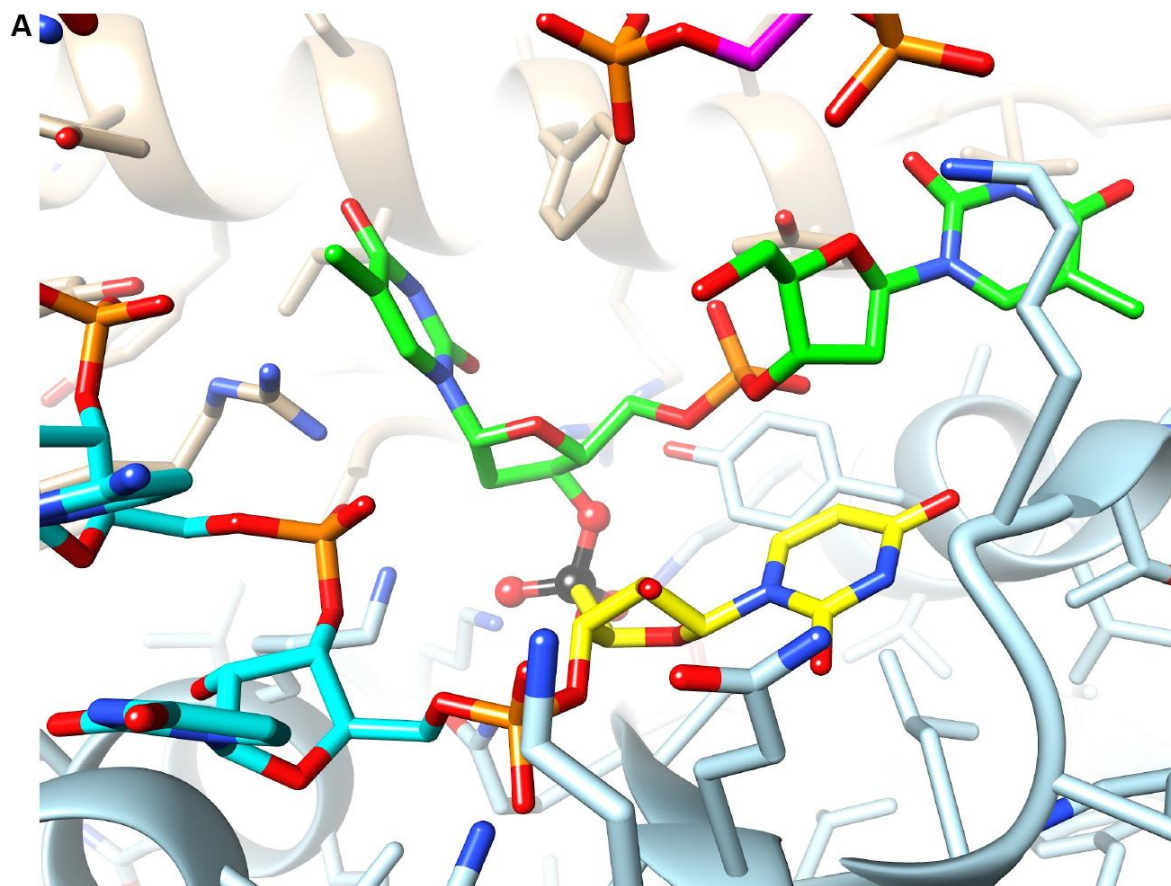
957    bars represent SEM.

959 **Figure 4. Model of inverted chimeric siRNA cleavage product within Ago2 complex. (A**)

960 Representation of the active KRAS guide strand with a 2dT 5'-overhang. KRAS guide siRNA

961 carbon atoms are in cyan, dTdT carbon atoms are in light green, carbon atoms of the 5'-terminal

962 U1 of the KRAS guide strand are in yellow, and carbon atoms of amino acids from the Ago2 MID

963 and PIWI domains are colored in light blue and tan, respectively. (**B**) Model depicting the KRAS

964 guide strand bound to Ago2 with the protein shown in a surface representation. Ago2 MID and

965 PIWI domain residues are colored in light blue and tan, respectively, the phosphorus atom of the

966 'former' 5'-terminal phosphate lodged at the MID Lys/Arg/Gln/Tyr binding pocket is highlighted in

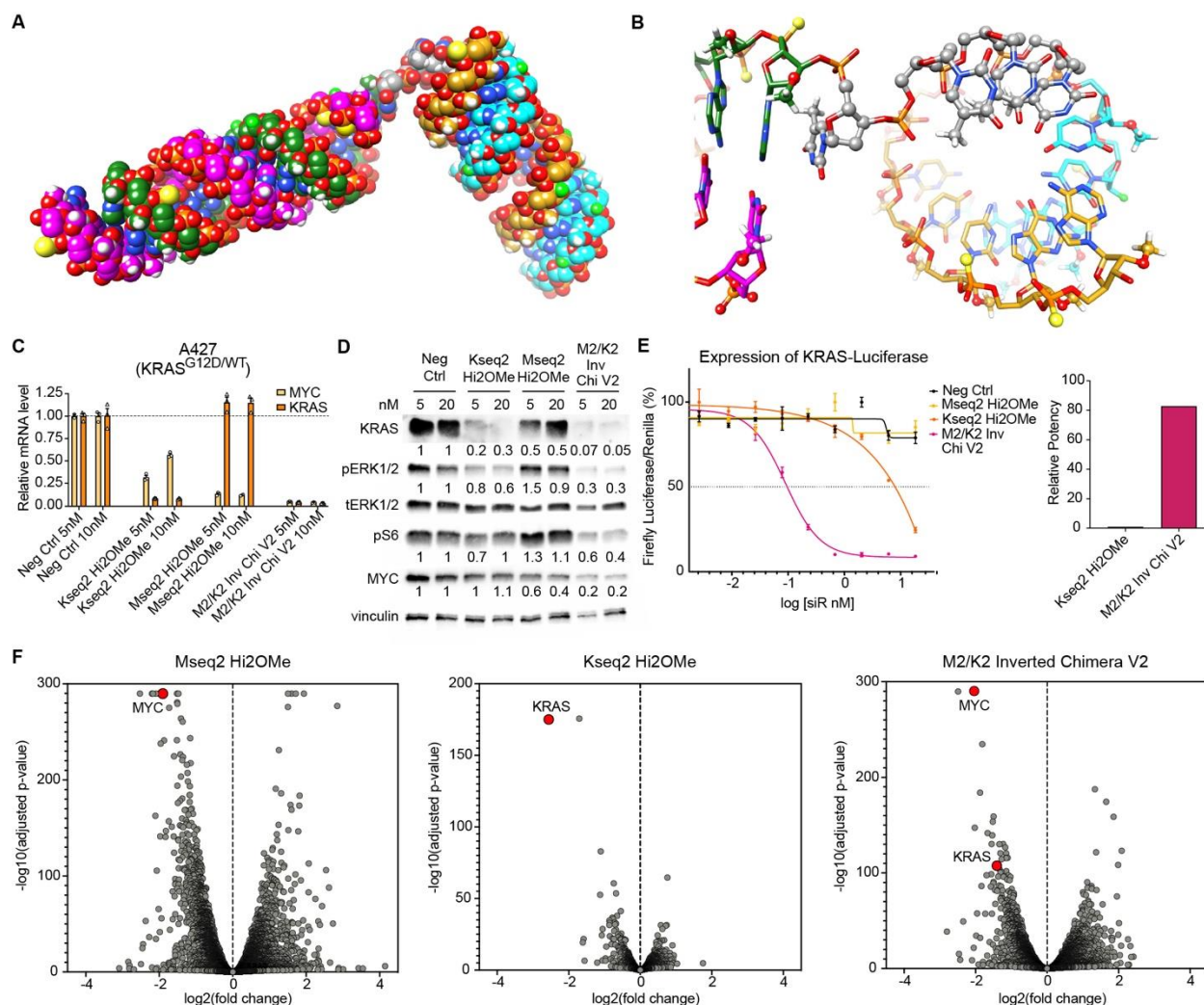967 black, and the strand with carbon atoms colored in purple is the targeted *KRAS* mRNA.

968

969

**Figure 5. Characterization of MYC/KRAS inverted chimeric siRNA with enhanced 2'OMe chemical modification.** (**A**) 3D space-filling model of the fully modified M2/K2 Inverted Chimera V2. Carbon atoms of the MYC guide strand are in magenta and carbon atoms of the passenger strand are in green. Carbon atoms of the KRAS guide strand are in cyan and carbon atoms of the passenger strand are in gold. The thymidine bridge is shown with carbon atoms in gray, 2'-fluorine atoms are light green, and phosphorothioate sulfur atoms are yellow. (**B**) Ball-and-stick model showing a portion of the inverted chimeric siRNA, with the KRAS G:P duplex viewed along the helical axis and carbon atoms of the kinked d(T)$_4$ bridge highlighted as gray spheres. The color code is the same as in (**A**). (**C**) Relative *MYC* and *KRAS* expression by RT-qPCR in A427 cells following treatment with the negative control (NC) siRNA, MYC Hi2OMe, KRAS Hi2OMe, and

981    M2/K2 Inverted Chimera V2 at 5 and 10nM for 72 hrs. Error bars represent SEM. (**D**) KRAS,

982    phospho-ERK1/2, total ERK1/2, phospho-S6, and MYC expression by Western blot in A427 cells

983    following treatment with the negative control siRNA, MYC Hi2OMe, KRAS Hi2OMe, and M2/K2

984    Inverted Chimera V2 at 5 and 20nM for 72 hrs. Relative expression values are shown below each

985    band for KRAS, phospho-ERK1/2, phospho-S6, and MYC. (**E**) Representative dose-response

986    curves and ED50s of KRAS-Firefly luciferase expression in A-431 KRAS-knockout cells treated

987    for four days with the NC siRNA, MYC Hi2OMe, KRAS Hi2OMe, and M2/K2 Inverted Chimera

988    V2. All Firefly-luciferase luminescence values were normalized with Renilla-luciferase

989    luminescence and expressed as a percentage. Error bars represent SEM. (**F**) RNA-sequencing

990    volcano plots showing all genes upregulated and downregulated in comparison to negative control

991    conditions following treatment of A427 cells with indicated siRNAs at 20nM for 24 hrs.
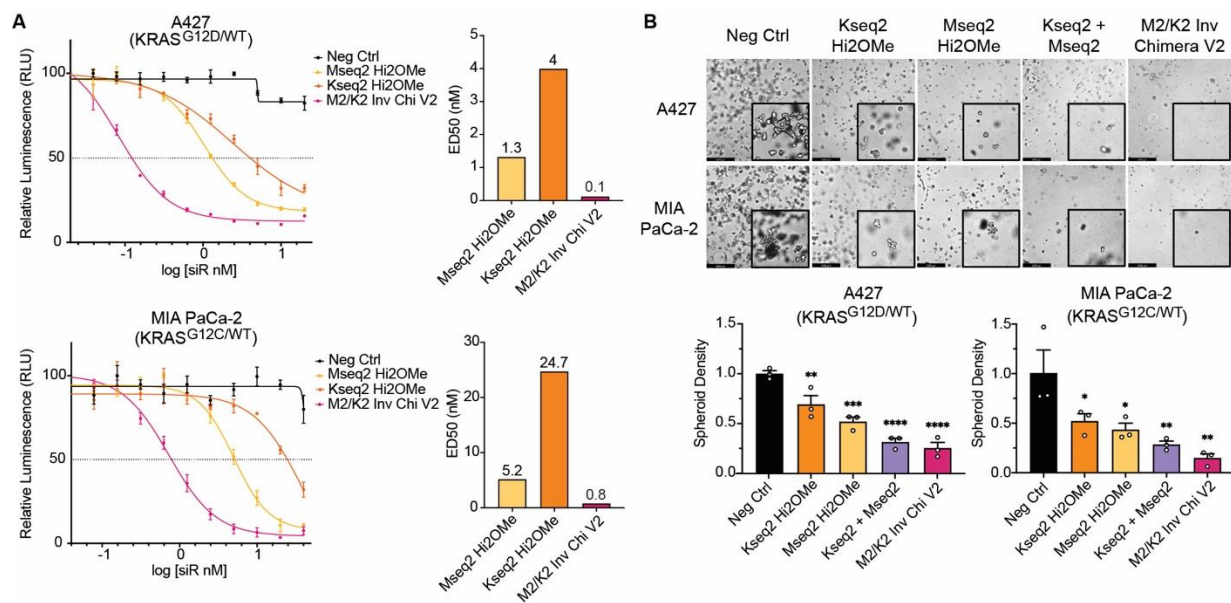
992

993

994

995

996

997

998

**Figure 6. Effects of M2/K2 inverted chimeric siRNA on cancer cell viability.** (**A**) Representative dose-response curves and ED50s for MIA PaCa-2 and A427 cells treated for six days with the negative control siRNA, MYC Hi2OMe, KRAS Hi2OMe, and M2/K2 Inverted Chimera V2. ED50s are shown in nM above the respective bar in the bar graphs on the right. Data are representative of three replicates and error bars represent SEM. (**B**) Representative images and quantification of spheroids in a tumorigenesis assay in Matrigel with A427 and MIA PaCa-2 cells. Images were taken with a 5x microscope objective. Scale bar, 498μm. Error bars represent SEM. One-way ANOVA was used for statistical comparisons. (****) = $p < 0.0001$, (***) = $p < 0.001$, (**) = $p < 0.01$, (*) = $p < 0.05$.
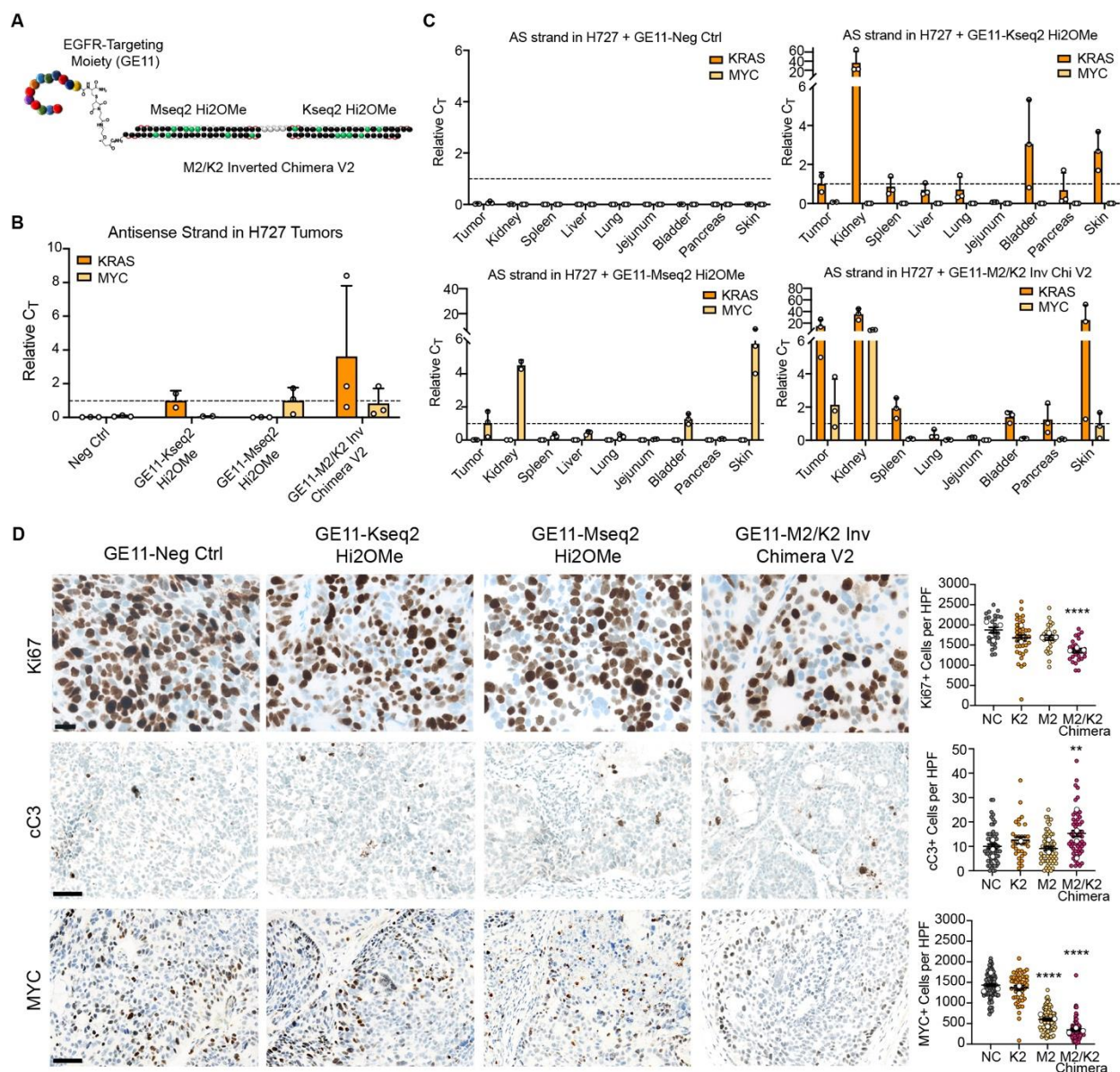
**Figure 7**. **Characterization of receptor-targeting ligand GE11**. (**A**) Structure of GE11-conjugated M2/K2 Inverted Chimera V2 (at the 3' end of the guide strand). (**B**) Relative abundance values of the MYC and KRAS antisense (AS, guide) strands in aggregate tumors of each treatment group. Relative values for the MYC guide strand were normalized to the GE11-MYC siRNA treatment group, and relative values for the KRAS guide strand were normalized to the GE11-KRAS siRNA treatment group. Error bars represent SEM. (**C**) Relative AS abundance values of the MYC and KRAS guide strands in aggregate tumors, kidneys, spleen, lung, jejunum, bladder, pancreas, and skin of each treatment group. Relative values for the MYC guide strand

1018  were normalized to the GE11-MYC siRNA treatment group, and relative values for the KRAS

1019  guide strand were normalized to the GE11-KRAS siRNA treatment group. Error bars represent

1020  SEM. (**D**) (left) Representative images of Ki67, cleaved caspase-3 (cC3), and MYC staining in

1021  paraffin-embedded sections of H727 tumors treated for seven days with siRNAs. Ki67 scale bar:

1022  20 µm. cC3 and MYC scale bars: 50 µm. (right) Quantification of the positive cells per high-

1023  powered field in sections of H727. Error bars represent SEM. Unpaired one-tailed t-test corrected

1024  for multiple comparisons with the Bonferroni method was used for statistical comparisons. (****)

1025  = p<0.0001. (**) = p<0.01.

1026
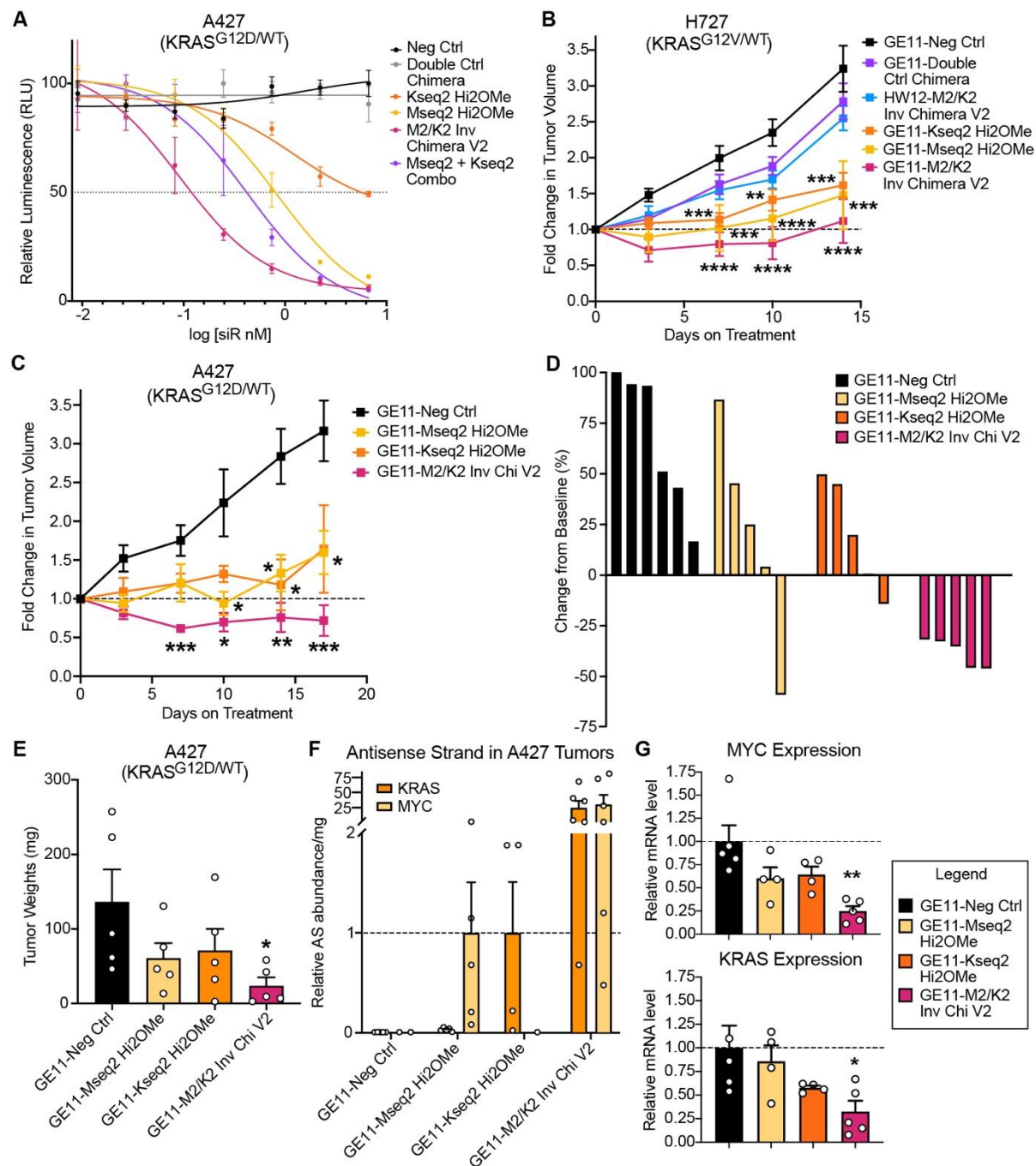
**Figure 8. In vivo activity and efficacy of M2/K2 inverted chimeric siRNA.** (**A**) Representative dose-response curves for A427 cells treated for six days with the negative control siRNA, double control siRNA, Mseq2 Hi2OMe, Kseq2 Hi2OMe, and M2/K2 Inverted Chimera V2. Error bars represent SEM. (**B**) Tumor growth curves showing average fold change in H727 tumor volume over 15 days (n=10 for all treatment groups). Error bars represent SEM. Unpaired one-tailed t-

1032  test corrected for multiple comparisons using the Bonferroni method was used for statistical

1033  comparisons. (**C**) Tumor growth curves showing average fold change in A427 tumor volume over

1034  21 days (n=6 for GE11-Neg Ctrl, n=5 for GE11-Mseq2 Hi2OMe, GE11-Kseq2 Hi2OMe, and

1035  GE11-M2/K2 Inverted Chimera V2).  Error bars represent SEM. Unpaired one-tailed t-test

1036  corrected for multiple comparisons using the Bonferroni method was used for statistical

1037  comparisons. (**D**) Percent change in A427 tumor volume for each mouse from baseline after eight

1038  days of siRNA treatment. (**E**) Tumor mass in all treatment groups following cross-sectional

1039  necropsy at day 21 (n=5 for all groups). Error bars represent SEM. Unpaired one-tailed t-test was

1040  used for statistical comparisons. (**F**) Relative abundance values of the MYC and KRAS antisense

1041  (guide) strands per mg of tumor of each treatment group. Relative values for the MYC guide

1042  strand were normalized to the GE11-MYC siRNA treatment group, and relative values for the

1043  KRAS guide strand were normalized to the GE11-KRAS siRNA treatment group. Error bars

1044  represent SEM. (**G**) Relative *MYC* and *KRAS* mRNA expression in the tumors of each treatment

1045  group (n=5 for the GE11-Neg Ctrl and GE11-M2/K2 Inverted Chimera V2 groups, n=4 for the

1046  GE11-Mseq2 and GE11-Kseq2 groups). Error bars represent SEM. Unpaired one-tailed t-test

1047  corrected for multiple comparisons using the Bonferroni method was used for statistical

1048  comparisons. (****) = $p<0.0001$. (***) = $p<0.001$. (**) = $p<0.01$. (*) = $p<0.05$.
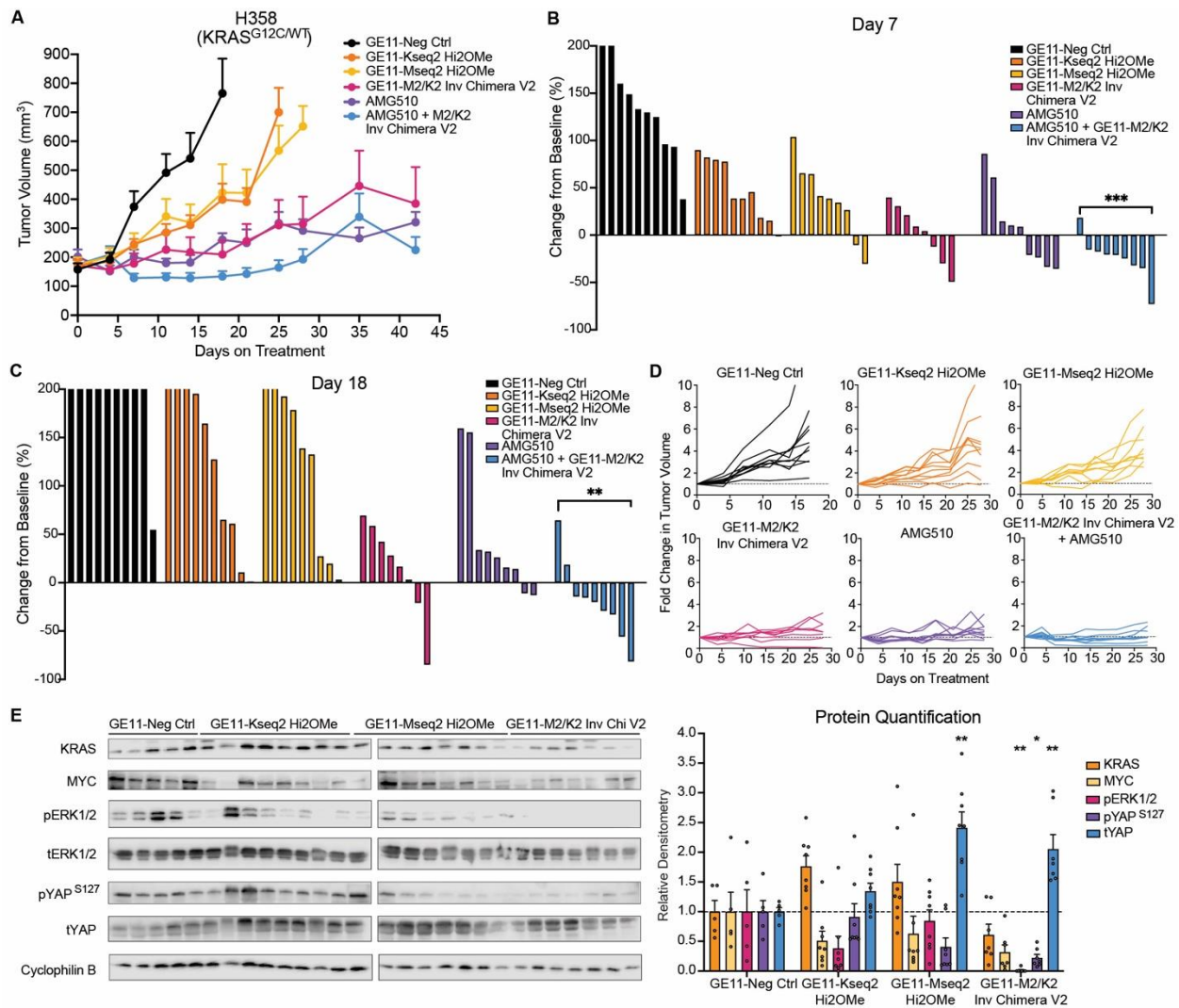
1049

**Figure 9. Long-term in vivo efficacy of M2/K2 inverted chimeric siRNA.** (**A**) Tumor growth

curves showing average fold change in H358 tumor volume over 42 days (n=7-10 for all treatment

groups). After 28 days, measurements were taken weekly. Error bars represent SEM. (**B**) Percent

change in H358 tumor volume for each mouse from baseline after seven days of siRNA treatment.

(**C**) Percent change in H358 tumor volume for each mouse from baseline after seventeen days of

siRNA treatment. (B-C) Two-tailed Fisher's exact test corrected for multiple hypothesis testing

using the Bonferroni method was used for statistical comparisons. (***) = $p<0.001$, (**) = $p<0.01$.

(**D**) Spider plots of fold changes in H358 tumor volume for every mouse in each treatment group

over 42 days. (**E**) KRAS, MYC, phospho-ERK1/2, total ERK1/2, phospho-YAP$^{S127}$, and total YAP

by Western blot in H358 tumors following treatment with GE11-conjugated negative control

1061 siRNA, MYC Hi2OMe, KRAS Hi2OMe, and M2/K2 Inverted Chimera V2. Tumors are ordered by

1062 responsiveness to treatment within each group, with strong responders in the beginning and

1063 resistant tumors at the end. Band intensities were quantified with Image Lab and relative band

1064 intensities (graph to the right) were calculated in comparison to negative control siRNA-treated

1065 tumors after normalization to cyclophilin B. Error bars represent SEM. Two-tailed Mann Whitney

1066 test corrected for multiple comparisons using the Bonferroni method was used for statistical

1067 comparisons. (**) = $p<0.01$, (*) = $p<0.05$.

1068

1069